ADVANCED ENERGY MATERIALS
www.advenergymat.de

# Triple A-Site Cation Mixing in 2D Perovskite-Inspired Antimony Halide Absorbers for Efficient Indoor Photovoltaics

*Noora Lamminen, Gopal Krishnamurthy Grandhi, Francesca Fasulo, Arto Hiltunen, Hannu Pasanen, Maning Liu, Basheer Al-Anesi, Alexander Efimov, Harri Ali-Löytty, Kimmo Lahtonen, Paavo Mäkinen, Anastasia Matuhina, Ana Belén Muñoz-García, Michele Pavone, and Paola Vivo**

**Antimony-based perovskite-inspired materials (PIMs) are solution-processable halide absorbers with interesting optoelectronic properties, low toxicity, and good intrinsic stability. Their bandgaps around 2 eV make them particularly suited for indoor photovoltaics (IPVs). Yet, so far only the fully inorganic $Cs_3Sb_2Cl_xI_{9-x}$ composition has been employed as a light-harvesting layer in IPVs. Herein, the first triple-cation Sb-based PIM (CsMAFA-Sb) in which the A-site of the $A_3Sb_2X_9$ structure consists of inorganic cesium alloyed with organic methylammonium (MA) and formamidinium (FA) cations is introduced. Simultaneously, the X-site is tuned to guarantee a 2D structure while keeping the bandgap nearly unchanged. The presence of three A-site cations is essential to reduce the trap-assisted recombination pathways and achieve high performance in both outdoor and indoor photovoltaics. The external quantum efficiency peak of 77% and the indoor power conversion efficiency of 6.4% are the highest values ever reported for pnictohalide-based photovoltaics. Upon doping of the P3HT hole-transport layer with F4-TCNQ, the power conversion efficiency of CsMAFA-Sb devices is fully retained compared to the initial value after nearly 150 days of storage in dry air. This work provides an effective compositional strategy to inspire new perspectives in the PIM design for IPVs with competitive performance and air stability.**

## 1. Introduction

Indoor photovoltaics (IPVs) have been recently recognized as the "next big trend" in photovoltaics[1] with a rapidly expanding market.[2,3] While commercial IPVs rely on hydrogenated amorphous silicon (a-Si:H),[4] perovskite-based photovoltaics have lately become a forefront IPV technology due to the impressive indoor power conversion efficiency (PCE(i)) as high as 40.1% at 1000 lux,[5] facile band gap tunability[6] allowing adaptation to different light sources and illuminance conditions, and straightforward and cost-effective solution processability.[7] Nevertheless, currently the most efficient perovskite-based IPVs employ absorbers containing lead cation ($Pb^{2+}$), which introduces toxicity hazards especially relevant in indoor scenarios, or air-unstable tin cation ($Sn^{2+}$).[8,9] Hence, exploring less toxic yet stable perovskite derivatives for IPVs is

N. Lamminen, G. K. Grandhi, A. Hiltunen, H. Pasanen, M. Liu, B. Al-Anesi, P. Mäkinen, A. Matuhina, P. Vivo
Hybrid Solar Cells
Faculty of Engineering and Natural Sciences
P.O. Box 541, Tampere University, Tampere FI-33014, Finland
E-mail: paola.vivo@tuni.fi

F. Fasulo, M. Pavone
Department of Chemical Sciences
University of Naples Federico II
Comp. Univ. Monte Sant'Angelo
Naples 80126, Italy

The ORCID identification number(s) for the author(s) of this article can be found under https://doi.org/10.1002/aenm.202203175.

© 2022 The Authors. Advanced Energy Materials published by Wiley-VCH GmbH. This is an open access article under the terms of the Creative Commons Attribution License, which permits use, distribution and reproduction in any medium, provided the original work is properly cited.

DOI: 10.1002/aenm.202203175

A. Hiltunen
Biodiversity Unit of the University of Turku
Yliopistonmäki (Vesilinnantie 5), Natura
University of Turku, Turku 20014, Finland

A. Efimov
Chemistry and Advanced Materials
Unit of Materials Science and Environmental Engineering
Faculty of Engineering and Natural Sciences
Tampere University
P.O. Box 541, Tampere 33014, Finland

H. Ali-Löytty
Surface Science Group
Photonics Laboratory
Tampere University
P.O. Box 692, Tampere University, Tampere FI-33014, Finland

K. Lahtonen
Faculty of Engineering and Natural Sciences
Tampere University
P.O. Box 692, Tampere FI-33014, Finland

A. B. Muñoz-García
Department of Physics "Ettore Pancini" University of Naples Federico II
Comp. Univ. Monte Sant'Angelo
Naples 80126, Italy



Check for updates
16146840, 2023, 4, Downloaded from https://onlinelibrary.wiley.com/doi/10.1002/aenm.202203175 by University of Turku, Wiley Online Library on [03/02/2023]. See the Terms and Conditions (https://onlinelibrary.wiley.com/terms-and-conditions) on Wiley Online Library for rules of use; OA articles are governed by the applicable Creative Commons License

16146840, 2023, 4, Downloaded from https://onlinelibrary.wiley.com/doi/10.1002/aenm.202203175 by University of Turku, Wiley Online Library on [03/02/2023]. See the Terms and Conditions (https://onlinelibrary.wiley.com/terms-and-conditions) on Wiley Online Library for rules of use; OA articles are governed by the applicable Creative Commons License

an urgent and highly challenging research goal. Low-dimensional perovskite-inspired materials (PIMs) based on Group VA cations, for example, antimony (III) ($Sb^{3+}$) and bismuth (III) ($Bi^{3+}$), are gaining increasing interest due to their significantly higher chemical stability and lower toxicity than $Sn^{2+}$ and $Pb^{2+}$ counterparts, respectively.[10] Their band gap of around 2 eV makes them particularly suitable for IPVs that can reach the maximum theoretical PCE(i) values of up to 50–60%.[3,4,11]

Sb-based PIMs form crystalline structures with $A_3Sb_2X_9$ stoichiometry, with A being the monovalent cation (like $Cs^+$) and X the halide anion (such as $I^-$). Two polymorphs are reported for $A_3Sb_2X_9$ PIMs, namely the 0D dimer and the 2D layered form.[12,13] While the 0D dimer is easily obtainable via solution-based synthesis at low temperature, on the other hand, it is not ideal for photovoltaic applications owing to its indirect band gap and poor charge-carrier transport.[14] Conversely, the 2D polymorph enables effective charge transport across the layers and has a direct bandgap but it is thermodynamically stable typically at high-temperatures.[12,15] Hence, several works have recently focused on how to promote the suppression of the 0D phase and the formation of the 2D layered one. This has been successfully accomplished via small A-site cation (e.g., $Cs^+$, $Rb^+$, $NH_4^+$) engineering and/or co-alloying at the X-site (e.g., $I^-$ with $Cl^-$).[15–19]

2D Sb-based absorbers have yielded solar cells with a respectable power conversion efficiency (PCE). The highest values of 2.5% ($Cs_3Sb_2I_9$)[20] and 3.3% ($MA_3Sb_2I_{9-x}Cl_x$ upon the introduction of bis(trifluoromethane)sulfonimide lithium (LiTFSI)[21]–PCE is 2.2% for pristine $MA_3Sb_2I_{9-x}Cl_x$[22]) in planar and mesoporous architectures, respectively, are among the best PCEs for Pb- and Sn-free perovskite solar cells. Surprisingly, despite the nearly ideal bandgaps of Sb-PIMs for indoor light-harvesting, currently only one Sb-PIM composition (the fully inorganic $Cs_3Sb_2Cl_xI_{9-x}$ with a bandgap of 2.05 eV)[4] has been investigated in IPVs, demonstrating a PCE(i) of 4–5%, that is, already comparable to that of commercially available a-Si:H devices. Albeit promising, these results highlight the large difference between the current PCE(i) values and their upper theoretical limit, in turn motivating the discovery of novel 2D Sb-PIM compositions suitable for IPVs.

All the Sb-PIM compositions reported so far comprise a single cation at the A-site, such as inorganic Cs or organic methylammonium (MA), except for the recent example of $FA_xCs_{3-x}Sb_2I_6Cl_3$ PIM,[23] including both Cs and formamidinium (FA) A-site cations. Such double cation mixing at the A-site can enhance the solar cell performance under 1-Sun illumination. These encouraging results on double A-site cation[23] and the striking performance of MA-based Sb-PIMs[21,22] have driven our strategy to further increase the compositional space of Sb-PIMs by a triple A-site cation mixing involving Cs, MA, and FA cations. In fact, we have targeted 2D structures with suitable bandgaps for IPV applications.

Herein, we report the first organic–inorganic triple-cation Sb-based PIM, $Cs_{2.4}MA_{0.5}FA_{0.1}Sb_2I_{8.5}Cl_{0.5}$ (referred to as CsMAFA-Sb), obtained by a facile solution synthesis. Our joint theoretical and experimental study demonstrates that the material has a 2D structure despite the presence of large MA and FA cations, enabled by the mixed iodide-chloride X-site anions. The I:Cl ratio is fine-tuned to guarantee an appropriate bandgap for indoor light harvesting. Planar *n–i–p* solar cells with CsMAFA-Sb absorber outperform the parent double-cation CsMA-Sb and CsFA-Sb based devices mostly due to a short-circuit current density ($J_{SC}$) and open-circuit voltage ($V_{OC}$) increase. CsMAFA-Sb leads to the highest values of PCE(i) (6.4%) and external quantum efficiency (EQE) (77%) ever reported for pnictohalide-based devices. Our comprehensive characterization at both film and device level provides a profound understanding of the charge extraction and recombination dynamics. Furthermore, it correlates them to the dark current, the shunt losses in the devices, and the defect density in the Sb-PIM films. Finally, we demonstrate that the incorporation of all the three A-site cations (Cs, FA, MA) in the Sb-PIM composition is the key to reducing the trap-assisted nonradiative recombination pathways and developing highly efficient devices.

This work promotes future compositional design efforts for the next-generation absorbers with low toxicity, intrinsically high stability, and low defect density for high-performance IPVs.

## 2. Results and Discussion

### 2.1. Design and Synthesis of CsMAFA-Sb PIMs

To form CsMAFA-Sb, we aimed at partially replacing the inorganic Cs of the parent $Cs_3Sb_2X_9$ PIM structure with the organic MA and FA cations. The desirable 2D layered phase of CsMAFA-Sb was achieved through a thorough composition engineering involving both A- and X-sites. Indeed, it is expected that the incorporation of large cations (MA and FA) pushes the $[SbI_6]^{3-}$ octahedra closer, thus promoting the formation of the 0D dimer phase instead of the 2D layered one.[24] Therefore, we targeted the inclusion of a sufficient amount of $Cl^-$ in the crystal structure of CsMAFA-Sb PIM as $Cl^-$ is known to favor the formation of the 2D phase.[19,22,23]

The solution-phase synthesis of the triple-cation Sb-PIM consists of a standard one-step spin-coating upon an appropriate selection of the metal halide precursors. The chloride anion can be in principle introduced through cesium chloride (CsCl), formamidinium chloride (FACl), or methylammonium chloride (MACl) precursor. We selected MACl, as it was successfully employed as a chloride source by Jiang et al. to form 2D layered Sb-PIMs,[22] while CsCl is known to cause solubility issues.[22] Moreover, MACl in the precursor solution may produce Sb PIM films with an improved quality.[22,25] The introduction of MACl simultaneously incorporates also MA in the crystal structure, thus promoting a dual-site (A- and X-sites) compositional engineering of Sb-PIMs. Overall, the precursor materials for CsMAFA-Sb are cesium iodide (CsI), formamidinium iodide (FAI), and MACl. More details on the synthesis of the triple-cation Sb-PIM are provided in the Supporting Information. The band gap of the parent composition $Cs_3Sb_2I_9$ (≈2.1 eV) is close to the optimum value for efficient indoor light harvesting,[4] thus preserving the original band gap is necessary for achieving IPVs with high PCE(i). Since excess Cl incorporation may alter the band gap of the resulting Sb-PIM,[21,22] we aimed at the lowest Cl:I ratio that enables the formation of the 2D phase.


© 2022 The Authors. Advanced Energy Materials published by Wiley-VCH GmbH

We first performed Cs- and MA-mixing at the A-site leading to double-cation Sb-PIM (CsMA-Sb) with composition $Cs_{3-x}MA_xSb_2I_{9-y}Cl_y$. To this aim, we mixed CsI, $SbI_3$ and MACl precursors (in DMF solutions) in 1.5:1.0:0.25, 1.5:1.0:0.5, 1.5:1.0:1.0 and 1.5:1.0:1.5 molar ratios. The minimum amount of MACl necessary for obtaining the CsMA-based Sb-PIM in a 2D layered structure was verified through X-ray diffraction (XRD) characterization of the as-obtained films. Next, $Cs_{3-z-x}MA_xFA_zSb_2I_{9-y}Cl_y$ (CsMAFA-Sb) films were fabricated with the above-optimized MACl quantity (fixed) and tunable CsI:FAI ratios (CsI:FAI:$SbI_3$:MACl = 1.2:0.3:1.0:1.5 and 0.75:0.75:1.0:1.5). Higher FA loadings resulted in yellow-colored films. A comprehensive structural, optical, and photovoltaic study of these films demonstrated that the organic–inorganic A-site mixing involving all the three cations (Cs, MA, and FA) is the key to high-performance devices. Thus, in the following sections, we focus on the detailed characterization of the layered triple-cation CsMAFA-Sb PIM.

### 2.2. Structure, Composition, and Morphology of Sb-PIMs with Hybrid A-Site Cations

The XRD patterns of CsMA-Sb films fabricated by spin-coating precursor solutions containing variable MACl:$SbI_3$ molar ratios and a constant CsI quantity (as described above) are shown in **Figure 1**a and Figure S1, Supporting Information. The standard XRD patterns of the 2D and 0D phases of Sb-PIMs are also

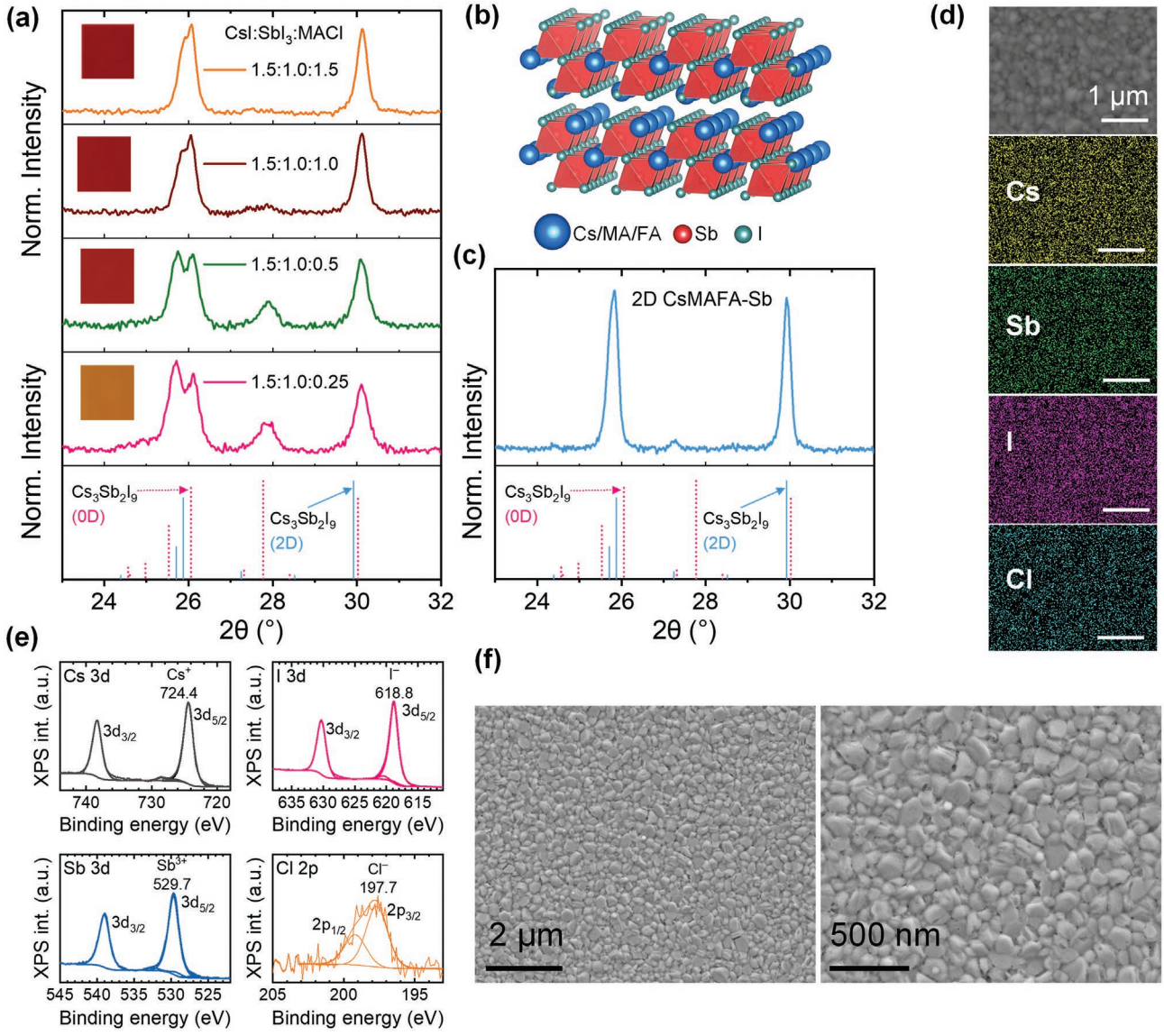


**Figure 1.** a) Evolution of XRD patterns of CsMA-Sb films from 0D to 2D structure with increasing MACl in CsI:$SbI_3$:MACl molar ratio. The images (under room light) of the corresponding films are shown in the insets. The color of the films changes gradually from yellow (0D) to dark red (2D) with the increase in MACl concentration. b) The crystal of 2D layered Sb-PIM with $A_3Sb_2I_9$ composition. c) XRD pattern of CsMAFA-Sb film along with the reference patterns for the 0D (reference code: 98-008-4989) and 2D (reference code: 04-009-5795) $Cs_3Sb_2I_9$. d) SEM-EDS color maps of Cs, Sb, I, and Cl of the triple cation PIM film. e) XPS spectra of Cs 3d, Sb 3d, I 3d, and Cl 2p for a CsMAFA-Sb film. f) Low and high-resolution SEM images of a CsMAFA-Sb film.


© 2022 The Authors. Advanced Energy Materials published by Wiley-VCH GmbH

16146840, 2023, 4, Downloaded from https://onlinelibrary.wiley.com/doi/10.1002/aenm.202203175 by University of Turku, Wiley Online Library on [03/02/2023]. See the Terms and Conditions (https://onlinelibrary.wiley.com/terms-and-conditions) on Wiley Online Library for rules of use; OA articles are governed by the applicable Creative Commons License

included in Figure 1a. While the XRD pattern of the layered phase (*P*3-*m*1 space group) contains only two prominent peaks between 25° and 30°, that of the 0D dimer (P63/*mmc* space group) contains four prominent peaks at 25.6°, 26.2°, 27.9° and 30.2°.[12] The yellow-colored film with the lowest MACl amount (i.e., $CsI:SbI_3:MACl = 1.5:1.0:0.25$) predominantly crystallizes in the 0D dimer (yellow) phase, as revealed by the two peaks in the 25–26° range and the characteristic peak at 27.9°. The peak splitting (at 25–26°) and the intensity of 27.9° peak both decreased for the film with the precursor ratio of 1.5:1.0:1.0. The actual Cl:I ratio in the resulting film increases up to 0.09 in this case, as determined by scanning electron microscopy (SEM)-energy dispersive X-ray spectroscopy (EDS). The 27.9° peak completely disappeared in the 1.5:1.0:1.5 case, confirming the structural transition to the layered phase at a higher MACl concentration (Cl:I = 0.12) (see Figure 1a). This sample has a composition of $Cs_{2.4}MA_{0.6}Sb_2I_{7.4}Cl_{0.9}$ according to SEM-EDS analysis. The optimum MACl concentration ($CsI:SbI_3:MACl = 1.5:1.0:1.5$) was selected for further mixing with FA cation at the A-site leading to the triple-cation CsMAFA-Sb structure (Figure 1b). The molar ratio of $CsI:FAI:SbI_3:MACl = 1.2:0.3:1.0:1.5$ enabled the formation of CsMAFA-Sb PIM in the desired 2D crystal structure, as shown in Figure 1c (see also Figure S2, Supporting Information). Rietveld refinement (goodness of fit is 1.29 and $R_{wp}$ is 2.4%) of the XRD pattern of this sample further confirmed that it crystallizes in the *P*-3*m*1 space group, that is, in the 2D layered phase (Figure S3, Supporting Information). The film stored in a dry air environment preserved its layered structure for more than 30 days, as shown in Figure S4, Supporting Information. The XRD peaks at ≈26° (doublet), 30° and 43° correspond to (003), (201), (022) and (220) crystal planes, respectively (see Figure 1c and Figure S2, Supporting Information). The appearance of not just the (00l) planes suggests that the $[SbI_6]^{3-}$ octahedral sheets have a random orientation on the substrate,[13] which offers an efficient charge collection compared to the case when the sheets fully align parallel to the substrate surface (the parallel orientation forbids the charge extraction when sandwiched between the charge extraction layers). Higher FAI loadings (e.g., $CsI:FAI:SbI_3:MACl = 0.75:0.75:1.0:1.5$) in the presence of the same MACl concentration did not result in the phase-pure 2D structure (Figure S5, Supporting Information).

The SEM-EDS study shows the uniform distribution of Cs, Sb, I, and Cl (Figure 1d) elements in CsMAFA-Sb and a bulk composition of $Cs_{2.4}(MA+FA)_{0.6}Sb_2I_{8.5}Cl_{0.5}$. The actual stoichiometry of the A-site organic cations of the film does not necessarily reflect that in their precursor solution.[26] Therefore, the composition of the organic part (MA, FA) of the film was quantified by nuclear magnetic resonance (NMR) spectroscopy.[26] A few identical Sb-PIM films were scrapped off to obtain a Sb-PIM powder. A known amount of the resultant powder was dissolved in an aliquot volume of deuterated DMSO, thus being able to use a common liquid state technique NMR. For the sake of comparison, the NMR spectra of FAI, MACl, and their mixtures with CsI and $SbI_3$ salts in deuterated DMSO were recorded as well. All the chemical shifts were referenced to the DMSO signal at 2.49 ppm for proton and 39.5 ppm for the carbon spectra. The combined NMR data are given in Table S1, Supporting Information. The molar ratio of MA to FA cations was found to be 4:1, as calculated from the integrals of the corresponding 1H NMR signals at 7.84 and 2.35 ppm, respectively (more details about the NMR data collection and analysis can be found in Figures S6–S12, Supporting Information). The molar MA:FA ratio obtained from the NMR studies, combined with the atomic composition achieved from SEM-EDS ($Cs_{2.4}(MA+FA)_{0.6}Sb_2I_{8.5}Cl_{0.5}$) allowed us to fully determine the composition of CsMAFA-Sb as $Cs_{2.4}MA_{0.5}FA_{0.1}Sb_2I_{8.5}Cl_{0.5}$. Interestingly, only a small portion of the MACl added to the precursor solution was incorporated into the sample. The Cl:I ratio (1:17) in CsMAFA-Sb that guarantees the crystallization in the pure 2D phase is much lower compared to the very high ratios (for instance, 3.5:1.0, 1:2, and 1:5) employed in earlier works[19,21–23] to secure the 0D→2D phase transition. The surface composition of the CsMAFA-Sb film determined by X-ray photoelectron spectroscopy (XPS) closely matches that of the bulk composition obtained by EDS, except for a higher Cs and slightly lower halide content (see the comparison between EDS and XPS compositions in **Table 1**). Such deviation in surface versus bulk composition may have been induced by the evaporation of volatile halides and organic FA/MA.[27]

**Table 1.** Bulk and surface atomic ratios of triple cation Sb PIM film from EDS and XPS data analysis.

| Element | EDS | XPS |
|---|---|---|
| Cs | 2.4 | 3.1 |
| Sb | 2 | 2 |
| I | 8.5 | 7.5 |
| Cl | 0.5 | 0.4 |

Only elements belonging to the CsMAFA-Sb PIM were detected in the XPS survey spectrum (Figure S13, Supporting Information). One chemical state was resolved for Cs (Cs $3d_{5/2}$ at 724.4 eV), Sb (Sb $3d_{5/2}$ at 529.7 eV), I (I $3d_{5/2}$ at 618.8 eV) and Cl (Cl $2p_{3/2}$ at 197.7 eV) corresponding to the valence states of $Cs^+$, $Sb^{3+}$, $I^-$ and $Cl^-$, respectively (Figure 1e and Table S2, Supporting Information).[27] Organic $MA^+$ (H—C—N bond) and $FA^+$ (N=C—N) could not be reliably differentiated from C 1s (Figure S14c, Supporting Information) due to overlapping signals from adventitious carbon (C—C/H, C—O, and O=C—O). N 1s (Figure S14f, Supporting Information) showed two peaks; one at 401.5 eV corresponding to $MA^+/FA^+$ (N—C) and another peak at 399.5 eV that appeared during XPS measurement and was therefore assigned as an X-ray effect.[28] Similar species have been previously observed to evolve during light soaking and attributed to $NH_3$ release.[27] In addition, a small amount of oxygen (2.8 at%, O 1s at 532.5 eV, (Figure S14d, Supporting Information) was detected on the surface of the film, which is likely due to hydration of the CsMAFA-Sb surface.[27]

The top-view SEM images of the 2D CsMAFA-Sb film show that the material spreads densely and uniformly over the substrate (Figure 1f). Moreover, the film is pinhole-free, with moderately large crystal grains, whose size is up to 250 nm. The surface roughness of the film was estimated by the Atomic-force microscopy (AFM) images, as shown in Figure S15, Supporting Information. The root-mean-square roughness ($R_q$) value of 22 nm, comparable to that of reported PIM films, indicates the good quality of the film with smooth morphology.


© 2022 The Authors. Advanced Energy Materials published by Wiley-VCH GmbH

16146840, 2023, 4, Downloaded from https://onlinelibrary.wiley.com/doi/10.1002/aenm.202203175 by University of Turku, Wiley Online Library on [03/02/2023]. See the Terms and Conditions (https://onlinelibrary.wiley.com/terms-and-conditions) on Wiley Online Library for rules of use; OA articles are governed by the applicable Creative Commons License

**Table 2.** Lattice parameters, stacking between layers ($d_1$ and $d_2$ in Figure S17, Supporting Information) at PBE level of theory and bandgap (indirect/direct) at HSE06 level of theory of the optimized 2D-$A_3Sb_2X_9$ PIMs structure.

| 2D-$A_3Sb_2X_9$ | Lattice parameters/f.u. [Å] | | | Stacking [Å] | | Band gap [eV] | |
|---|---|---|---|---|---|---|---|
| | a | b | c | $d_1$ | $d_2$ | Indirect | Direct |
| $Cs_3Sb_2I_9$ | 8.30 | 8.30 | 10.23 | 6.95 | 3.28 | 1.72 | 1.77 |
| $Cs_{2.4}FA_{0.6}Sb_2I_9$ | 8.55 | 8.37 | 10.24 | 6.93 | 3.31 | 1.78 | 1.82 |
| $Cs_{2.4}MA_{0.6}Sb_2I_9$ | 8.43 | 8.35 | 10.28 | 6.97 | 3.31 | 1.75 | 1.80 |
| $Cs_{2.4}MA_{0.5}FA_{0.1}Sb_2I_9$ | 8.45 | 8.36 | 10.27 | 6.96 | 3.31 | 1.75 | 1.80 |
| $Cs_{2.4}MA_{0.5}FA_{0.1}Sb_2I_{8.5}Cl_{0.5}$ | 8.42 | 8.32 | 10.24 | 6.94 | 3.29 | 1.81 | 1.85 |

### 2.3. First-Principles Calculations

We investigated the structural and electronic features of the synthesized 2D CsMAFA-Sb PIMs via state-of-the-art density functional theory (DFT)-based computations. Starting from the parent $Cs_3Sb_2I_9$ composition, we considered the partial replacement of Cs with MA, FA or both, leading to the double- and triple A-site cations ($Cs_{2.4}FA_{0.6}Sb_2I_9$, $Cs_{2.4}MA_{0.6}Sb_2I_9$, $Cs_{2.4}MA_{0.5}FA_{0.1}Sb_2I_9$) and mixed I/Cl anions ($Cs_{2.4}MA_{0.5}FA_{0.1}Sb_2I_{8.5}Cl_{0.5}$). Structural and computational details are reported in the Supporting Information.

Relaxed optimized structures of the inorganic 2D-layered $Cs_3Sb_2I_9$ PIM and its hybrid organic–inorganic derivatives are featured in Figure S16, Supporting Information. An overview of the computed lattice constants and structural parameters for these systems are collected in **Table 2**. All the mixed CsMAFA-Sb PIMs show the typical 2D layered phase of $A_3Sb_2I_9$.[13,29–33] On one hand, the double-cation CsFA-Sb has a more pronounced difference between the a and b lattice constants that differ by 0.18 Å because of a lattice elongation of 0.25Å (≈3%) along the *a*-axis. On the other, the CsMA-Sb PIM has only a mild impact on structural parameters: this double-cation PIM shows only a difference of 0.08 Å between *a* and *b* lattice constants and an increment of ≈0.5% along the *c*-axis. Including both organic cation (FA/MA) and Cl-anions results to parameters very close to the parent material, also preserving the stacking between $SbI_8$ octahedra ($d_1$ and $d_2$ in Figure S17, Supporting Information)

Previous DFT analysis pointed out that the difference between the direct and indirect band gaps of 2D $Cs_3Sb_2I_9$ PIM is small, thus this material shows a nearly direct band gap behavior.[13,29–33] To achieve a high device performance, we are interested to preserve the nature of the $Cs_3Sb_2I_9$ band gap. We have analyzed the electronic properties of the investigated mixed PIMs derivatives in terms of their projected density of states (pDOS) (**Figure 2**) and the band energy structures (Figures S18 and S19, Supporting Information). The direct and indirect band gap values reported in Table 2 highlight that the quasi-direct behavior is retained in all the mixed inorganic–organic PIMs. However, only for $Cs_{2.4}MA_{0.5}FA_{0.1}Sb_2I_{8.5}Cl_{0.5}$ composition, where the A-site cation mixing involves all the three cations (i.e., Cs, MA, FA) and I and Cl are mixed at the X-site, there is an increase of ≈0.1 eV (≈5%) for both the direct and indirect band gap, together with a decreased difference between them (≈0.04 eV). Additionally, as seen in Figure 2, the explored PIMs-compositions present an electronic behavior very similar to that of $Cs_3Sb_2I_9$. In all cases, the valence band is given by the typical s–p interaction from the hybridization of Sb(5s) atomic orbitals and I(5p) atomic orbitals, while the conduction band is dominated by the strong p–p interactions resulting from the overlap of I(5p)–Sb(5p).[29,30] It can be also seen that the MA/FA cations, as the Cs-cations, do not directly contribute to the valence band maximum (VBM) and conduction band maximum (CBM).

Overall, our DFT results highlight that the triple-cation $Cs_{2.4}MA_{0.5}FA_{0.1}Sb_2I_{8.5}Cl_{0.5}$ Sb-PIM is predicted to form a stable 2D layered structure and, additionally, also possesses nearly direct band gap features and a suitable band gap value for efficient indoor light-harvesting.

### 2.4. Optical and Photophysical Characterization of Triple-Cation CsMAFA-Sb Films

The absorption spectrum (**Figure 3**a) of CsMAFA-Sb has an onset at ≈600 nm, below which a steep increase in absorbance values occurs. To experimentally demonstrate the direct or quasi-direct band gap behavior of CsMAFA-Sb suggested by the DFT study, we performed a Tauc plot analysis on the absorption spectrum (see Figure S20-1 and Table S3, Supporting Information). The small energy difference (0.07–0.12 eV) between the indirect and direct band gaps confirms our theoretical findings of the nearly direct or quasi-direct band gap nature[13,19,22] of CsMFA-Sb, which is sufficient for strong light absorption.[13] The band gap of the 2D CsMAFA-Sb (2.1 eV) is the same as for the layered $Cs_3Sb_2I_9$ (2.09 eV),[20] and it is very suitable for indoor light harvesting.[4]

A broad and weak emission band with a maximum at 792 nm was observed for CsMAFA-Sb (Figure 3a), which can be assigned either to the self-trapped exciton (STE) induced emission or a combination of STE and defect-related emission, as proposed for other Sb-based PIMs.[20,34,35] The photoexcited state lifetimes of Sb-PIMs, such as $Cs_3Sb_2I_9$, are known to be short.[20] Indeed, the time-resolved photoluminescence (TRPL) decay of CsMAFA-Sb PIM films also showed a lifetime <1 ns, approaching the time resolution limit of the instrument (see the comparison between the TRPL decay curve and the instrument response function, IRF, in Figure 3b). Hence, to probe the charge-carrier dynamics of our Sb-PIM and gain insights into the excited-state of the material, we conducted ultrafast transient absorption (TA) spectroscopy measurements. Figure 3c shows the TA spectra of CsMAFA-Sb PIM film,


© 2022 The Authors. Advanced Energy Materials published by Wiley-VCH GmbH

16146840, 2023, 4, Downloaded from https://onlinelibrary.wiley.com/doi/10.1002/aenm.202203175 by University of Turku, Wiley Online Library on [03/02/2023]. See the Terms and Conditions (https://onlinelibrary.wiley.com/terms-and-conditions) on Wiley Online Library for rules of use; OA articles are governed by the applicable Creative Commons License

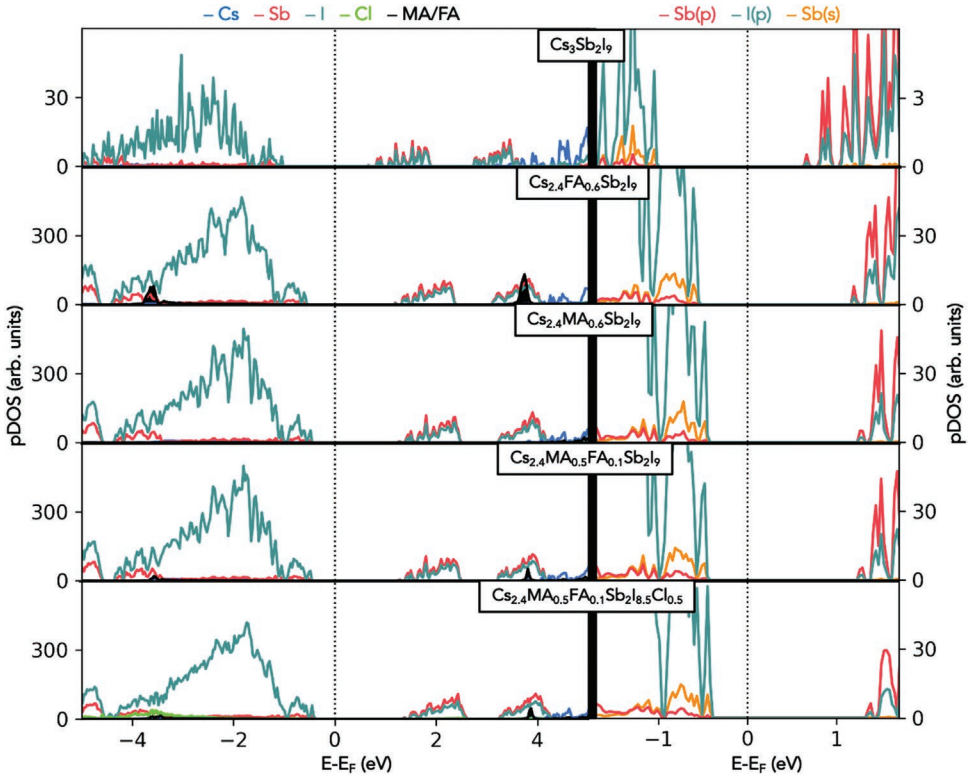


**Figure 2.** Projected density of states (pDOS) of the 2D-$A_3Sb_2X_9$ PIMs with A = Cs, FA, MA and X = I, Cl. Color code left panel: Cs (blue), Sb (red), I (teal), Cl (green), MA/FA (black) (on left). Color code right panel: p-states Sb (red), s-states Sb (orange), p-states I (teal).

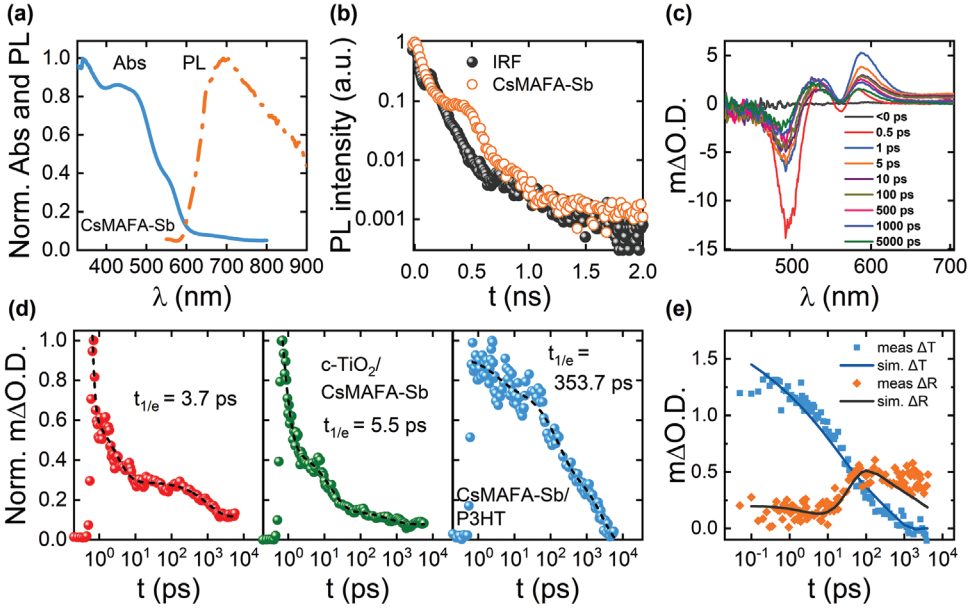


**Figure 3.** a) Absorption and PL ($\lambda_{ex}$ = 405 nm) spectra of CsMAFA-Sb film. b) TRPL decay of CsMAFA-Sb at 405 nm excitation and monitored at the emission maximum. The IRF is also shown. c) Ultrafast TA spectra of glass/CsMAFA-Sb, at 400 nm excitation with an excitation power of 100 µW. d) TA decays of glass/CsMAFA-Sb (left), glass/c-$TiO_2$/CsMAFA-Sb (middle) and glass/CsMAFA-Sb /P3HT (right), which were monitored at 600 nm. The dashed lines represent the corresponding fits with a tri-exponential function: $\Delta O.D. = A_1 \exp\left(-\frac{t}{\tau_1}\right) + A_2 \exp\left(-\frac{t}{\tau_2}\right) + A_3 \exp\left(-\frac{t}{\tau_3}\right)$. e) TR and TA signals at 700 nm fitted using the thin-film interference and diffusion simulation. Diffusion coefficient is 0.3 $cm^2\ s^{-1}$ and the corresponding mobility is 12 $cm^2\ V^{-1}\ s^{-1}$.


© 2022 The Authors. Advanced Energy Materials published by Wiley-VCH GmbH

16146840, 2023, 4, Downloaded from https://onlinelibrary.wiley.com/doi/10.1002/aenm.202203175 by University of Turku, Wiley Online Library on [03/02/2023]. See the Terms and Conditions (https://onlinelibrary.wiley.com/terms-and-conditions) on Wiley Online Library for rules of use; OA articles are governed by the applicable Creative Commons License

excited at 400 nm, at different time delays. The TA spectra have two similar characteristics: i) a strong photo-bleaching (PB) feature (negative signal) centered around one exciton resonance (480 nm); and ii) two photoinduced absorption (PIA) features (positive signals) centered around 530 and 600 nm. A minor bleaching feature was also observed at 550 nm, possibly overlapping with the positive peaks at 530 and 600 nm. When the sample was excited at 530 nm, it also produced the 480 nm bleaching, confirming that the two bleaching signals arise from the same material instead of two different materials.

The featured asymmetric shape of TA with PIA at longer wavelength and PB at shorter wavelength is ascribed to the Stark effect induced bathochromic-shift and wideness of the exciton resonance, respectively, as has been observed for 2D $Cs_3Sb_2I_9$.[36] To investigate the charge recombination dynamics, we studied the TA decay of CsMAFA-Sb film (Figure 3d), monitored at 600 nm. The decay can be fitted well with a tri-exponential function (see the fitting results in Table S4, Supporting Information). We attribute the ultrafast and middle-fast components to the combination of self-trapping and nonradiative recombination and the slow component to the radiative recombination of STEs.[37,38] The observation of a fast (self-) trapping of the charge carriers was also confirmed by the transient reflectance (TR) spectroscopy study on CsMAFA-Sb (Figure S21, Supporting Information). This phenomenon could partially explain the $V_{OC}$ losses at a low light intensity of the corresponding photovoltaic devices.[39]

To study the charge recombination at the interface between CsMAFA-Sb and the charge-transport layers ($TiO_2$, electron-transport layer, and poly(3-hexylthiophene-2,5-diyl) (P3HT), hole-transport layer, similarly as in the photovoltaic devices discussed in the next section), we evaluated the TA decay dynamics of glass/c-$TiO_2$/CsMAFA-Sb and glass/CsMAFA-Sb/P3HT samples. In the analysis, we refer to an effective lifetime,[40] $t_{1/e}$, where $\Delta O.D.(t_{1/e}) = \Delta O.D.(0)/e$. The TA decay of glass/c-$TiO_2$/CsMAFA-Sb film exhibits a short effective lifetime (<6 ps), suggesting that the electron extraction process from the conduction band (CB) of the CsMAFA-Sb to that of the $TiO_2$ layer is not very efficient. On the other hand, the TA decay of glass/CsMAFA-Sb/P3HT shows a very long effective lifetime (353.7 ps), which is more than two orders of magnitude higher than that of glass/c-$TiO_2$/CsMAFA-Sb. This clearly hints that the hole transfer process dominates the interfacial charge recombination process in CsMAFA-Sb, similarly as in conventional Pb-based halide perovskites.[41]

The charge carrier diffusion coefficient and mobility were estimated by fitting the TR signal using the diffusion and thin-film interference models at 600–750 nm probe wavelengths (see Figure 3e and Figure S22, Supporting Information). The shorter wavelengths were more impacted by the trapping and therefore were deemed unreliable for the diffusion fit. The samples showed quite complex behavior in time-resolved measurements and therefore the diffusion coefficient of 0.3 $cm^2\ s^{-1}$ and the corresponding mobility of 12 $cm^2\ V^{-1}\ s^{-1}$ should be considered as an order-of-magnitude estimate. Nevertheless, the reasonable carrier mobility value of CsMAFA-Sb PIM estimated by TR falls in the range of mobility values (0.8–2.3 $cm^2\ V^{-1}\ s^{-1}$) reported for some other well-known PIMs (such as silver iodobismuthates, $Cs_2AgBiBr_6$, and $Cu_2AgBiI_6$) for photovoltaic applications.[42–44] The charge-carrier mobility of the CsMAFA-Sb film could be further enhanced by enlarging the grain size (see the top-view SEM images in Figure 1f) upon a careful optimization of the film processing conditions.[45,46]

### 2.5. Photovoltaic Performance

The performance of photovoltaic devices employing a CsMAFA-Sb light-harvesting layer was first evaluated by characterizing them under 1-Sun (AM 1.5 G, 100 mW $cm^{-2}$) illumination. To demonstrate that the mixing of all three organic and inorganic cations (Cs, MA, and FA) at the A-site is crucial to maximizing the solar cell performance, we fabricated two reference devices with double-cation CsMA-Sb and $Cs_{3-x}FA_xSb_2I_{9-y}Cl_y$ (CsFA-Sb) absorbers. CsMA-Sb was already introduced in the previous sections, as it represented the first step for the synthesis of CsMAFA-Sb. For the preparation of CsFA-Sb, the Cl:I ratio in the precursor solution was gradually increased until the desired 2D layered structure was obtained (see Figure S23 and Figure S20-2, Supporting Information, for the XRD patterns and absorption spectra, respectively), with a similar approach as the one we adopted for CsMA-Sb synthesis (the corresponding XRD and absorption data can be found in Figure S1 and Figure S20-3, Supporting Information). All the three kinds of devices (CsMA-, CsFA-, and CsMAFA-Sb based), fabricated in an *n–i–p* planar architecture, had "FTO/c-$TiO^2\ s^{-1}$b-PIM/P3HT/Au" structure, where c-$TiO_2$ (compact $TiO_2$) and P3HT (poly(3-hexylthiophene-2,5-diyl)) are the electron- and hole-transport layer (ETL and HTL), respectively. The device fabrication details are provided in the Supporting Information. **Figure 4**a shows the cross sectional view of a typical CsMAFA-Sb device (the thickness of CsMAFA-Sb layer is ≈210 nm). The statistical distribution of the PCE values of CsMA-, CsFA- and CsMAFA-Sb devices under 1-Sun illumination is displayed in Figure 4b, while the box charts of the fill factor (FF), $J_{SC}$ and $V_{OC}$ are provided in Figure S24, Supporting Information. The PCE of the champion CsMAFA-Sb device is 2.47%, whereas much lower values are detected for the best CsMA- (1.0%) and CsFA-Sb (0.66%) cells (see **Table 3**). The current density (*J*)–voltage (*V*) curves (both reverse and forward bias scans) of the champion CsMAFA-, CsMA-, and CsFA-Sb devices are shown in Figure 4c and Figure S25a,b, Supporting Information.

The highest PCE (2.47%) of CsMAFA-Sb devices is the same as that of inorganic $Cs_3Sb_2I_9$-based cells (2.48%[20]), with identical structure except the absorber, which still represents the state-of-the-art PCE of planar devices with an $A_3Sb_2X_9$ light-harvesting layer (with A being an inorganic or organic cation). However, a striking difference emerges when comparing the average PCE of CsMAFA-Sb (2.17%) and $Cs_3Sb_2I_9$ (1.29%) cells, which more realistically highlight the performance of the devices. In the case of the triple-cation devices, a standard deviation of ±0.17% is obtained, which is much smaller than that of $Cs_3Sb_2I_9$ devices (±0.46%), indicating the excellent reproducibility of the figure of merits of CsMAFA-Sb cells. The higher PCE values of CsMAFA-Sb devices versus those of the double cation (CsMA-Sb, CsFA-Sb) ones mainly arise from the enhanced $J_{SC}$ and $V_{OC}$. The improved $J_{SC}$ values of CsMAFA-Sb cells stem from high charge collection (see the


© 2022 The Authors. Advanced Energy Materials published by Wiley-VCH GmbH

16146840, 2023, 4, Downloaded from https://onlinelibrary.wiley.com/doi/10.1002/aenm.202203175 by University of Turku, Wiley Online Library on [03/02/2023]. See the Terms and Conditions (https://onlinelibrary.wiley.com/terms-and-conditions) on Wiley Online Library for rules of use; OA articles are governed by the applicable Creative Commons License

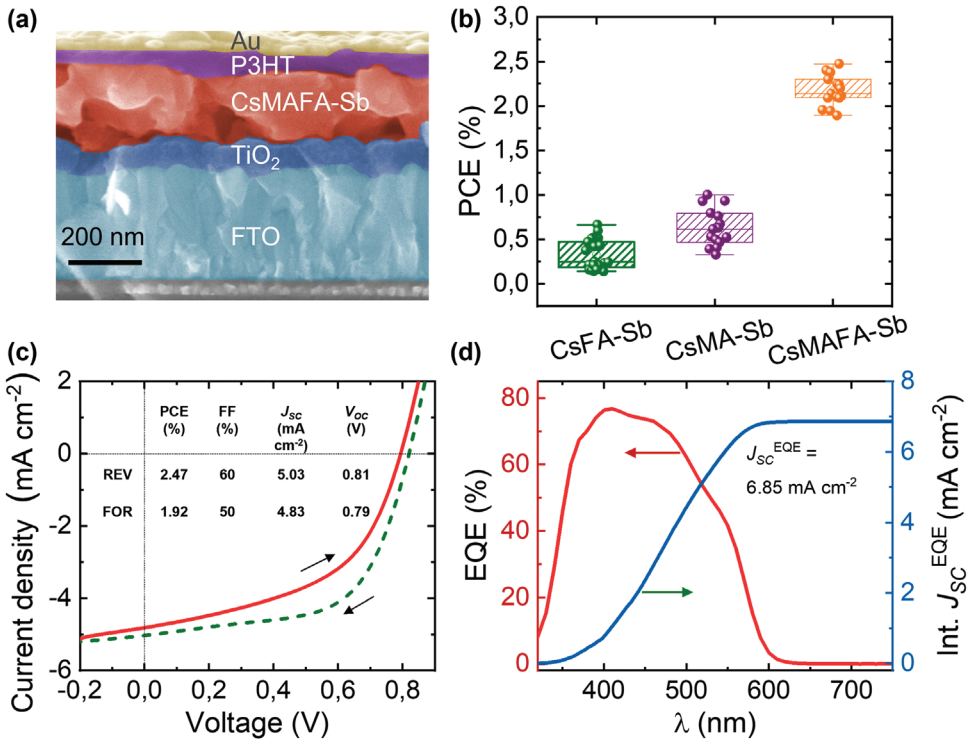


**Figure 4.** a) Cross sectional SEM image of a CsMAFA-Sb photovoltaic cell. b) Statistical distribution (over 15 devices) of the photovoltaic parameters of CsFA-Sb, CsMA-Sb, and CsMAFA-Sb devices under 1-Sun illumination. c) *J–V* curves (reverse and forward bias scans) of the best CsMAFA-Sb device under 1-Sun illumination. d) EQE spectrum and the integrated $J_{SC}^{EQE}$ curve of the device in Figure S25c, Supporting Information.

comparison of EQE spectra of the three devices in Figure S26, Supporting Information), boosted charge transport, and reduced non-radiative recombination.[47] The $V_{OC}$ (0.85 V) of the champion CsMAFA-Sb device is among the highest values ever reported for Sb-pnictohalide-based devices (see **Table 4**).[48] The low CsMAFA-Sb|P3HT interfacial recombination of the photogenerated holes at the interface, demonstrated by the high effective lifetime of 354 ps (Figure 3d), can partially explain the reduced $V_{OC}$ losses (average $V_{OC}$ = 0.80 ± 0.03 V) in the case of triple cation-Sb devices compared to the double cation-Sb (average $V_{OC}$ = 0.52–0.59 ± 0.05 V) and even to $Cs_3Sb_2I_9$ devices (0.63 ± 0.09 V),[20] also comprising P3HT as the HTL. Also, the crystalline grain size of the CsMAFA-Sb (244 nm) film is larger than those of CsMA-Sb (159 nm) and CsFA-Sb (134 nm) (see Figure S27, Supporting Information), in turn mitigating the recombination losses and enhancing the $V_{OC}$ of CsMAFA-Sb devices.[49] Regarding the FFs, CsMAFA-Sb devices display modest values (average and highest values are 50.3 ± 6.5% and 61.5%, respectively), which is typical for Sb-based PIM devices (see Table 4), in turn highlighting the need for further device interface engineering (e.g., thickness and film quality of HTL, ETL, and/or absorber).

**Table 3.** Average (15 devices) photovoltaic parameter values of CsMA-, CsFA-, and CsMAFA-Sb devices.

| Photovoltaic device | PCE [%] | FF [%] | $J_{SC}$ [mA cm$^{-2}$] | $V_{OC}$ [V] |
|---|---|---|---|---|
| CsMAFA-Sb | 2.17 ± 0.17 | 50 ± 6.2 | 5.87 ± 0.69 | 0.80 ± 0.03 |
| CsMA-Sb | 0.63 ± 0.21 | 64.2 ± 3.0 | 1.86 ± 0.45 | 0.52 ± 0.05 |
| CsFA-Sb | 0.33 ± 0.16 | 62.1 ± 3.4 | 1.25 ± 0.29 | 0.59 ± 0.05 |

We also explored how the selection of the HTL affects the performance of CsMAFA-Sb cells. We adopted well-known HTLs, poly[bis(4-phenyl)(2,4,6-trimethylphenyl)amine (PTAA) and 2,2″,7,7″-tetrakis[*N*,*N*-di(4-methoxyphenyl)amino]-9,9′-spirobifluorene (Spiro-OMeTAD), to be compared with P3HT and we also verified if the introduction of an HTL is at all beneficial (HTL-free sample) for maximizing the overall performance (see Figure S28, Supporting Information). In agreement with our earlier findings,[20] P3HT appears to be the best HTL for *n–i–p* planar Sb PIM-based devices. All the photovoltaic parameters are enhanced for P3HT cells. In particular, the average $V_{OC}$ (0.80 ± 0.03 V) is much higher than that of PTAA (0.60 ± 0.1 V), Spiro-OMeTAD (0.58 ± 0.1 V) or HTL-free (0.44 ± 0.14 V) devices, suggesting that the best energy level alignment between the valence band of CsMAFA and the HOMO of the HTL occurs when P3HT is selected.

The *J–V* curves (both reverse and forward bias scans) of a representative CsMAFA-Sb device, whose PCE (2.30%) closely matches the average PCE value of 2.17%, are shown in Figure S25c, Supporting Information. The device exhibits a small hysteresis between the two scans, as reported for $Cs_3Sb_2I_9$ devices earlier.[19,20] The EQE spectrum (Figure 4d) closely matches the absorption spectrum (see Figure 3a) of the light absorbing layer. The peak value is 77%, which is the highest EQE value ever reported for both planar (see Table 4) and mesoporous[19,21,50] Sb-based photovoltaic devices. The $J_{SC}$ value extracted from the EQE data ($J_{SC}^{EQE}$ = 6.85 mA cm$^{-2}$, as


© 2022 The Authors. Advanced Energy Materials published by Wiley-VCH GmbH

16146840, 2023, 4, Downloaded from https://onlinelibrary.wiley.com/doi/10.1002/aenm.202203175 by University of Turku, Wiley Online Library on [03/02/2023]. See the Terms and Conditions (https://onlinelibrary.wiley.com/terms-and-conditions) on Wiley Online Library for rules of use; OA articles are governed by the applicable Creative Commons License

**Table 4.** Reported peak EQE values and photovoltaic parameters of Sb PIM-based solar cells in a planar device architecture and comparison with this work. The values for the champion devices are given in brackets.

| Absorber composition | Peak EQE [%] | PCE [%] | FF [%] | $J_{SC}$ [mA cm$^{-2}$] | $V_{OC}$ [V] | Ref. |
|---|---|---|---|---|---|---|
| $Rb_3Sb_2I_9$ | ≈30 | 0.66 ± 0.09 (0.66) | 56.5 ± 2.2 (56.9) | 1.66 ± 0.28 (2.11) | 0.52 ± 0.02 (0.55) | Harikesh et al. Ref. [18] |
| $FACs_2Sb_2I_6Cl_3$ | ≈35 | 0.76 ± 0.07 (1.05) | 53.6 ± 2.8 (61.6) | 2.40 ± 0.14 (2.88) | 0.58 ± 0.01 (0.59) | Choi et al. Ref. [23] |
| $Cs_3Sb_2I_9$ | ≈35 | 1.21 | 55.8 | 3.55 | 0.61 | Umar et al. Ref. [15] |
| $Cs_3Sb_2I_9$ | ≈40 | 1.26 ± 0.18 (1.49) | 37.1 ± 2.7 (38.9) | 4.62 ± 0.71 (5.31) | 0.68 ± 0.04 (0.72) | Singh et al. Ref. [55] |
| $Cs_3Sb_2I_9$ | ≈50 | 1.29 ± 0.46 (2.50) | 49.2 ± 3.9 (54.9) | 3.98 ± 0.8 (5.04) | 0.63 ± 0.09 (0.80) | Hiltunen et al. Ref. [20] |
| $Rb_yCs_{3-y}Sb_2I_{9-X}Cl_X$ | ≈59 | 2.28 ± 0.16 (2.46) | 56 ± 3.0 | 4.77 ± 0.36 | 0.85 ± 0.2 (0.88) | Guo et al. Ref. [48] |
| $Cs_{2.4}MA_{0.5}FA_{0.1}Sb_2I_{8.5}Cl_{0.5}$ | 77% | 2.14 ± 0.20 (2.47) | 50.3 ± 6.5 (61.5) | 5.86 ± 0.70 (7.14) | 0.80 ± 0.03 (0.85) | This work |

shown in Figure 4d) is only slightly lower than that obtained from the *J–V* curves ($J_{SC}$ *J–V* = 7.14 mA cm$^{-2}$). Indeed, the 4.4% mismatch between $J_{SC}^{EQE}$ and $J_{SC}$ *J–V* values is within the acceptable range of 5%.[51]

We also monitored the shelf-life stability of the unencapsulated CsMAFA-Sb devices in the air (15% RH) at 25 °C for over three months (Figure S29, Supporting Information). The device retains 86% of its initial PCE after the first 28 days, owing to a small loss in its $J_{SC}$ and $V_{OC}$. This is consistent with the stability trend earlier reported for $Cs_3Sb_2I_9$ devices fabricated with P3HT HTL.[20] Nevertheless, at longer storage times (i.e., after one month) the device's PCE keeps dropping reaching a plateau after 60 days. The PCE trend nearly follows that of $J_{SC}$. The instability of the triple-cation solar cells may be attributed to the degradation of the CsMAFA-Sb absorber at the CsMAFA-Sb|P3HT interface. To improve the device stability, we aimed at optimizing this interface by doping P3HT with 2,3,5,6-tetrafluoro-7,7,8,8 tetracyanoquinodimethane (F4-TCNQ) additive. Our strategy was inspired by related works on the enhanced stability of perovskite solar cells upon F4-TCNQ doping of the HTL.[52,53] Also in the case of a CsMAFA-Sb PIM-based device, the F4-TCNQ doping of P3HT layer triggers a very remarkable enhancement of the device stability (Figure S29, Supporting Information). The PCE even increases after 100 days of storage and still retains its initial value after 149 days of storage. This is majorly contributed by a progressive increase in FF and $V_{OC}$, which could arise from gradual F4TCNQ doping of the HTL that improves its conductivity and enhances the charge extraction.[54] The drop in $J_{SC}$ (30%) in this case is significantly reduced compared to that of the device with pristine (undoped) P3HT (60%). This can be attributed to long-term uniform doping and reduced degradation of the absorber upon the F4-TCNQ-driven hydrophobic protection of the PIM layer underneath the HTL.[53] The P3HT doping approach to boost the shelf-lifetime of CsMAFA-Sb cells is an important contribution from this work, as it allows us to overcome a relevant and well-known weakness of Sb-PIM devices, that is, the modest air stability of the interface between Sb-PIM and P3HT.[20]

The EQE profile of the device better matches the white light-emitting diode (WLED) spectrum than the AM 1.5 G solar spectrum (**Figure 5**a), which hints at lowered non-absorbing photon loss in the devices under WLED illumination. Moreover, the high EQE of the CsMAFA-Sb device (Figure 4d) suggests the possibility of achieving a good performance under low-intensity indoor light illumination.[56] The *J–V* curves at 1000 and 200 lux illumination are shown in Figure 5b. Under 1000 lux, the device delivers a champion PCE(i) of 6.37%, and the corresponding FF, $J_{SC}$ and $V_{OC}$ values are 52%, 102 µA cm$^{-2}$ and 0.55 V, respectively. The 6.37% PCE(i) is the highest value ever reported for pnictohalides (5.52%[57] is the previous PCE(i) record, as shown in Table S5, Supporting Information). Figure 5c shows that the CsMAFA-Sb devices exhibit an average PCE(i) of 5.06% at 1000 lux. The $J_{SC}$ variation with light intensity provides an understanding of the dominant recombination mechanism at short-circuit conditions.[4] The exponent, $\alpha$, as $J_{SC} \propto I^{\alpha}$, can be determined by the log–log plot of $J_{SC}$ versus light intensity (I) (see **Figure 6**a). The value of $\alpha \approx 1$ suggests that defect-assisted recombination takes place in the CsMAFA-Sb device but through a fixed number of carrier trapping centers. The linear variation of $J_{SC}$ with the light intensity down to 100 lux also indicates that the charge collection efficiency of the device remains nearly unchanged regardless of the illumination intensity. We propose that a high EQE, which corresponds to effective charge extraction, is the key to achieving high PCE(i) values at 200 and 1000 lux indoor light.

The highest indoor $V_{OC}$ of 0.6 V, on pair with the best value ever reported for PIM-based IPVs,[58] was generated from CsMAFA-Sb devices. The open-circuit voltage decay (OCVD) trends help to shed light on the differences in the charge recombination processes in the three devices. The discharging time of the CsMAFA-Sb device is almost double than that of the CsMA-Sb and CsFA-Sb devices (Figure 6b), suggesting slower photogenerated charge recombination in the CsMAFA-Sb device. The electron lifetime of the devices was estimated from the open-circuit voltage decay (OCVD) curves using the following model:[59] $\tau_n = -\frac{k_B T}{e}\left(\frac{dV_{OC}}{dt}\right)^{-1}$, where $\tau_n$ is the electron lifetime, $k_B$ is the Boltzmann constant, $T$ is the temperature (K), $e$ is the elementary charge, and $t$ is the time after turning off the illuminating light. The $\tau_n$ is higher for the CsMAFA-Sb device than for the other two devices over the $V_{OC}$ range (Figure S30, Supporting Information), which can be attributed to reduced interfacial recombination between the absorber and the charge transport layers owing to a lower defect density.[60]

The $V_{OC}$ (0.55 V) of the champion device is significantly lower than the corresponding value under 1-Sun illumination (0.75 V). The reduction in $V_{OC}$ under indoor light can be estimated using the following expression:[61]


© 2022 The Authors. Advanced Energy Materials published by Wiley-VCH GmbH

16146840, 2023, 4, Downloaded from https://onlinelibrary.wiley.com/doi/10.1002/aenm.202203175 by University of Turku, Wiley Online Library on [03/02/2023]. See the Terms and Conditions (https://onlinelibrary.wiley.com/terms-and-conditions) on Wiley Online Library for rules of use; OA articles are governed by the applicable Creative Commons License

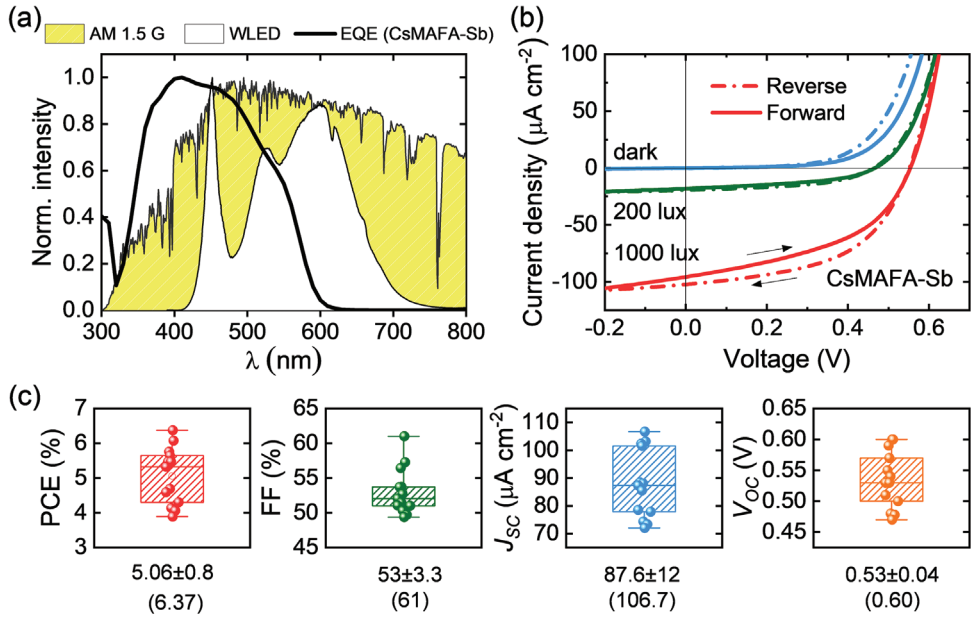


**Figure 5.** a) Comparison between the normalized EQE spectrum of CsMAFA-Sb photovoltaic cell, AM 1.5G (1-Sun) and WLED spectra. b) *J–V* curves (reverse and forward bias scans) of the CsMAFA-Sb cell under WLED (200 and 100 lux) illumination and in dark. c) Statistical distribution of the photovoltaic parameters of CsMAFA-Sb IPV cells under 1000 lux WLED illumination. The average and highest photovoltaic parameter values of the IPV devices are provided under the corresponding box plot.

$$\Delta V_{OC} = \frac{n_{ID} k_B T}{q} \ln \frac{I_{1-Sun}}{I_{WLED}} \quad (1)$$

where $n_{ID}$, $k_B$, $T$ and $q$ are diode ideality factor, Boltzmann constant (=1.38 × $10^{-23}$ J $K^{-1}$), temperature (=298 K) and electron charge (=1.6 × $10^{-19}$ J), respectively. $I_{1-Sun}$ and $I_{WLED}$ are the incident intensities of the 1-Sun and WLED light, respectively. By substituting $n_{ID}$ = 1 (the case of only radiative recombination), $I_{1-Sun}$ (100 mW $cm^{-2}$) and $I_{WLED}$ (0.092 and 0.46 mW $cm^{-2}$ at 200 and 1000 lux, respectively) values into the above expression, we estimated the $V_{OC}$ loss ($\Delta V_{OC}$) values of 0.18 and 0.14 V at 200 and 1000 lux, respectively. These values are lower than the ones obtained experimentally, that is, 0.29 V at 200 lux and 0.20 V at 1000 lux. Nevertheless, it should be noted that a voltage $V_{OC}$ loss of ≈0.2 V is unavoidable due to a significant reduction in the illumination intensity, as it has been observed even in highly promising IPV devices.[61,62] To understand the additional voltage loss in the case of CsMAFA-Sb IPV devices, the dependency of $V_{OC}$ on WLED intensity was studied, as shown in Figure 6c. The slope of the semi-log plot between $V_{OC}$ and WLED intensity equals $n_{ID}k_BT/q$. The extracted $n_{ID}$ value of ≈2 indicates that the recombination majorly occurs via the non-radiative pathways, which can be a combination of self-trapping of the exciton (evident from TA decay analysis) and charge-carrier trapping (feeble PL and very short radiative/excited-state lifetime). Therefore, the prevalent non-radiative recombination pathways cause the additional $V_{OC}$ loss in CsMAFA-Sb IPVs.

Another notable aspect of these devices under low-light illumination is their enhanced FF value of 53 ± 3.3% compared to the 50 ± 6.2% achieved under 1-Sun illumination. The improvement is particularly evident for the champion device—the FF increases from 43% (1-Sun) to 50–53% (200 and 1000 lux). The shunt resistance ($R_{sh}$) is known to influence the FF of photovoltaic cells more under low-lighting than in high light intensity conditions.[63,64] The $R_{sh}$ value (extracted from *J–V* curves) drastically increases from 390 Ω $cm^2$ at 1-Sun to 32 000 (1000 lux) and 81 000 Ω $cm^2$ (200 lux). Typically, under extremely low-light intensity, for instance at 200 lux, the PCE(i) can be much lower than at 1000 lux due to additional recombination pathways.[4] The high $R_{sh}$ values of CsMAFA-Sb device enable, instead, to harvest also the very low-intensity light efficiently. The device exhibits a remarkable performance under 200 lux with a PCE(i) of 4.73%. CsMAFA-Sb devices show a nearly constant FF trend in the 200–1000 lux illumination range (Figure 6d), and only an 11% loss in FF (with respect to the value at 1000 lux) at 100 lux. This is impressive considering the typical abrupt fall in FF (ascribed to the device shunting effect) observed when lowering the WLED light intensity in the case of $Cs_3Sb_2I_{9-x}Cl_x$ IPV devices.[4] The reduced number of photogenerated carriers at low light intensities implies that the defect (point and interstitial defects) density in the absorber is the key to maximizing the PCE(i) of the devices.[65] In particular, as the defect centers induce trap-assisted non-radiative recombination, the trap density directly affects both the $V_{OC}$ and the *FF*.[15,66–68] Hence, we assume that CsMAFA-Sb -Sb films have fewer trap sites than CsMA-Sb and CsFA-Sb. To experimentally prove our hypothesis, we evaluated the trap densities at the Sb-PIM|P3HT interface for the three devices (CsMA-Sb, CsFA-Sb, and CsMAFA-Sb) through the space-charge limited current (SCLC) method by fabricating hole-only devices with architecture "ITO/PEDOT:PSS/Sb-PIM/P3HT/$MoO_3$/Au."[69] The trap-filled limit voltage ($V_{TFL}$) is the bias onset at which the current sharply increases, corresponding to the trap-filling region of the dark *J–V* curves of the devices. As expected, the CsMAFA-Sb


© 2022 The Authors. Advanced Energy Materials published by Wiley-VCH GmbH

16146840, 2023, 4, Downloaded from https://onlinelibrary.wiley.com/doi/10.1002/aenm.202203175 by University of Turku, Wiley Online Library on [03/02/2023]. See the Terms and Conditions (https://onlinelibrary.wiley.com/terms-and-conditions) on Wiley Online Library for rules of use; OA articles are governed by the applicable Creative Commons License

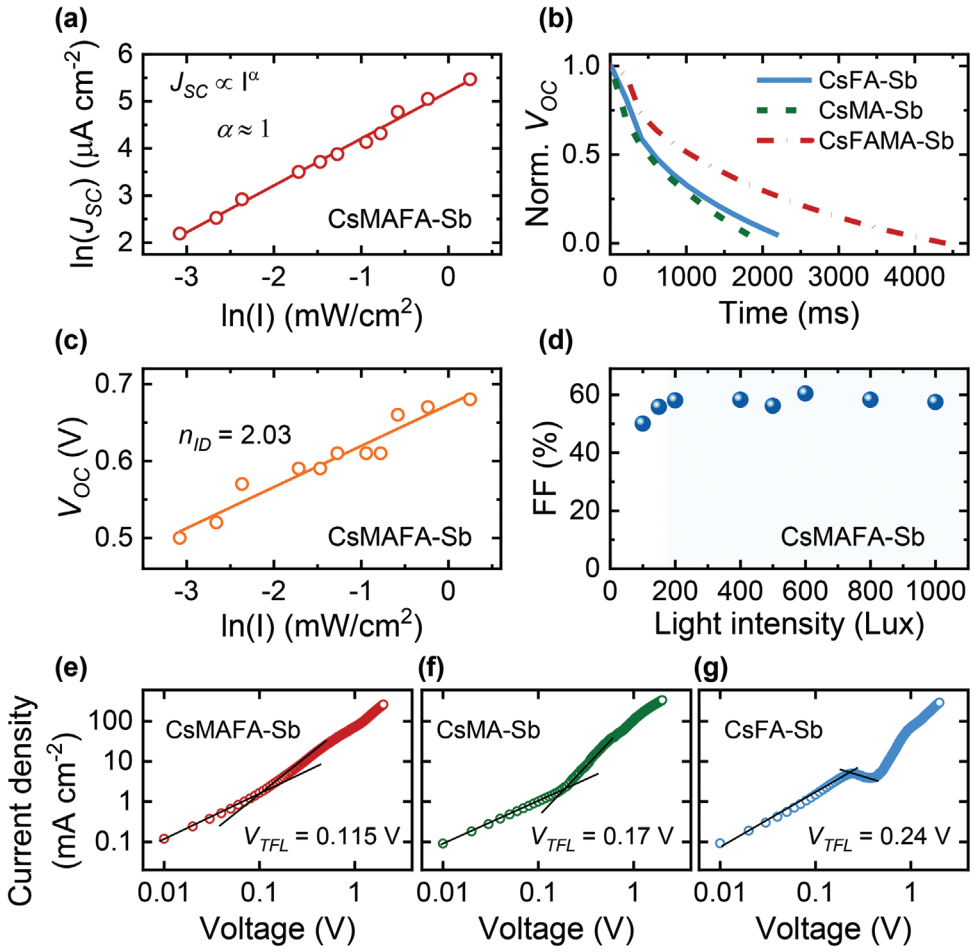


**Figure 6.** a) Log–log plot of $J_{SC}$ trend of the CsMAFA-Sb device versus WLED light intensity. b) Normalized open circuit voltage decay (OCVD) curves of the three devices, recorded after turning off (at $t = 0$) the WLED (1000 lux intensity) illumination. c) A semi-log trend of $V_{OC}$ of the CsMAFA-Sb device versus WLED light intensity. d) Variation of FF in CsMAFA-Sb device versus WLED light intensity. e–g) Dark *J–V* curves (on a log–log scale) of the hole-only devices (ITO/PEDOT:PSS/Sb-PIM/P3HT/$MoO_3$/Au) with the $V_{TFL}$ (trap-filled limit voltage) kink points.

PIM device exhibits the lowest $V_{TFL}$ value (0.115 V) among the three devices (Figure 6e–g), which leads to the lowest hole trap density ($N_{trap} = 3.97 \times 10^{15}$ cm$^{-3}$) compared to CsMA-Sb ($N_{trap} = 6.14 \times 10^{15}$ cm$^{-3}$) and CsFA-Sb ($N_{trap} = 8.67 \times 10^{15}$ cm$^{-3}$) devices. This confirms that the A-site organic–inorganic mixing in CsMAFA-Sb PIM leads to reduced defect density in the film, which could be attributed to its larger grain size versus CsMA-Sb and CsFA-Sb (see Figure S27, Supporting Information).

A low reverse dark current is also essential for a promising indoor performance of the devices. Indeed, the ratio between the dark current and the photogenerated current is considered a figure of merit for the IPV device performance.[60] The lowest dark current value of 1 μA cm$^{-2}$ at −1 V (extracted from the *J–V* curves measured in the −1 to +1 V range) was obtained for a CsMAFA-Sb device (Figure S31, Supporting Information). However, the average reverse dark current (7 μA cm$^{-2}$) is nearly 13–15 times lower than the photogenerated current ($J_{SC}^{avg} = 88$ μA cm$^{-2}$ and $J_{SC}^{max} = 107$ μA cm$^{-2}$), which prevented the recombination of all the charge carriers generated under indoor light and ensured a maximum PCE(i) of 6.37%. Such a small dark current also partially explains the relatively large $V_{OC}$ values[61] of the CsMAFA-Sb devices obtained under 1-Sun (0.80 ± 0.03 V) and indoor light (0.53 ± 0.05 V) illuminations. Both $J_{SC}$ (102 μA cm$^{-2}$) and $V_{OC}$ (0.55 V) of the champion CsMAFA-Sb device are significantly higher than the values reported for the champion $Cs_3Sb_2I_{9-x}Cl_x$ device (76 μA cm$^{-2}$, 0.47 V)[4] under the same light intensity of 1000 lux. This further supports the significance of the mixing of Cs sites with MA and FA organic cations in the Sb-PIM layer in reducing the non-radiative recombination in the CsMAFA-Sb devices compared to CsMA- and CsFA-Sb and $Cs_3Sb_2I_{9-x}Cl_x$ counterparts.

## 3. Conclusions

In summary, we have designed and synthesized a 2D antimony-based PIM, $Cs_{2.4}MA_{0.5}FA_{0.1}Sb_2I_{8.5}Cl_{0.5}$ (CsMAFA-Sb), through a triple cation mixing at the A-site. This strategy leads to CsMAFA-Sb *n–i–p* planar solar cells with higher efficiency than those employing the corresponding double cation PIMs (i.e., CsMA-Sb and CsFA-Sb), mostly due to enhanced $J_{SC}$ and $V_{OC}$ (as high as 0.86 V). The remarkable EQE peak of 77% achieved


© 2022 The Authors. Advanced Energy Materials published by Wiley-VCH GmbH

16146840, 2023, 4, Downloaded from https://onlinelibrary.wiley.com/doi/10.1002/aenm.202203175 by University of Turku, Wiley Online Library on [03/02/2023]. See the Terms and Conditions (https://onlinelibrary.wiley.com/terms-and-conditions) on Wiley Online Library for rules of use; OA articles are governed by the applicable Creative Commons License

with CsMAFA-Sb devices is the highest value ever reported for planar and mesoscopic Sb-based pnictohalide-based solar cells. The doping of the HTL layer (i.e., P3HT) with hydrophobic F4-TCNQ additive enables overcoming a known issue of inorganic Sb-based solar cells, namely the modest shelf-lifetime of the devices. Upon F4-TCNQ doping, the devices fully retain their initial PCE after 149 days of storage in dry air.

When the CsMAFA-Sb absorber is adopted in indoor photovoltaics, a record PCE(i) of 6.4% at 1000 lux and an impressive FF (50%) at very low intensities (100 lux) are achieved. Our comprehensive theoretical and experimental characterization of CsMAFA-Sb reveals that the compositional strategy of mixing inorganic Cs sites with both MA and FA organic cations is beneficial to achieve films with low defect density, which in turn reduces the $V_{OC}$ losses, particularly relevant at low-intensity indoor lighting. This work highlights the importance of A-site cation engineering in emerging lead-free perovskites and PIMs and opens new avenues (e.g., exploring other alkali and/or organic cations) for designing efficient and air-stable absorbers for indoor photovoltaics.

## 4. Experimental Section

*Materials*: Methylammonium chloride (MACl, 99.99%) and formamidinium iodide (FAI, 99.99%) were purchased from Greatcell Solar Materials. Antimony (III) chloride ($SbCl_3$, ≥99.95%), chlorobenzene (anhydrous, 99.8%), fuming (>37%) hydrochloric acid (HCl), titanium diisopropoxide bis(acetylacetonate) 75 wt% in 2-propanol, 2-propanol (anhydrous 99.5%), and poly(3,4-ethylenedioxythiophene)-poly(styrenesulfonate) (PEDOT:PSS, 1.3 wt% dispersion in H2O, conductive grade) were acquired from Sigma-Aldrich. Cesium iodide (CsI, 99.999%) was purchased from ABCR. Antimony iodide ($SbI_3$, 99.999%) was purchased from Fisher. *N*,*N*-dimethylformamide (DMF, anhydrous 99.8%) was acquired from Alfa Aesar. Poly(3-hexylthiophene-2,5-diyl) (P3HT, electronic grade, regioregular) was purchased from Rieke Metals. The 2,3,5,6-tetrafluoro-7,7,8,8 tetracyanoquinodimethane (F4-TCNQ) dopant was purchased from Ossila. All the chemicals were used as received, without any further purification.

*CsMA-Sb PIM*: The CsMA-Sb PIMs were prepared by mixing $SbI_3$, CsI and MACl (in DMF solutions) in molar ratios of 1.0:1.5:0.25, 1.0:1.5:0.5, 1.0:1.5:1.0 and 1.0:1.5:1.5. The ratio of 1.0:1.5:2.0 was also prepared but, as it did not dissolve completely under stirring, it was not further studied (nor for higher MACl ratios). The optimal ratio to obtain the desired 2D layered structure was determined through XRD to be 1.0:1.5:1.5, including 150 mol% of MACl compared to the amount of $SbI_3$.

*CsMAFA-Sb PIM*: The $Cs_{2.4}MA_{0.5}FA_{0.1}Sb_2I_{8.5}Cl_{0.5}$ precursor was obtained by mixing $SbI_3$, CsI, MACl and FAI (in DMF solution) in the molar ratio 1.0:1.2:1.5:0.3, with 150 mol% of MACl and 30 mol% of FAI compared to the amount of $SbI_3$.

*CsFA-Sb PIM*: The CsFA-Sb PIMs were prepared by mixing $SbI_3$, $SbCl_3$, CsI and FAI (in DMF solutions) in the molar ratios 0.97:0.03:1.20:0.30, 0.93:0.07:1.20:0.30, 0.87:0.13:1.20:0.30, 0.80:0.20:1.20:0.30 and 0.73:0.27:1.20:0.30. The optimal ratio to obtain the desired 2D layered structure was determined though XRD to be 0.73:0.27:1.20:0.30 of $SbI_3$, $SbCl_3$, CsI and FAI, respectively.

The concentration of all precursors was 444 mg $mL^{-1}$. All precursors were prepared inside an $N_2$-filled glovebox. The precursors were stirred with magnetic stirring for at least 4 h before use, to dissolve all the powders completely.

*Solar Cell Fabrication*: The solar cells were fabricated onto fluorine-doped tin oxide (FTO) coated substrates (TEC15 2.2 mm thick from Greatcell Solar Materials or pre-cut and etched ones from OPV tech). The TEC15 substrates were cut into 2 × 2 cm pieces and patterned by etching. The etching was performed by coating the desired area with a thin layer of zinc powder and submerging the substrate in 2 M hydrochloric acid solution for 5 min. The excess zinc was removed by brushing while still in the solution. The rest of the substrate was protected with tape (Scotch Magic tape) during the whole etching process. After etching the tape was removed and the substrates were cleaned by brushing with soap (2% Mucasol) and water. Subsequently, the substrates were cleaned by a 15-min sonication in ultra-pure water, acetone and 2-propanol and dried with an $N_2$ flow.

A compact titanium dioxide ($TiO_2$) layer was deposited onto the cleaned and etched substrates by spray pyrolysis. The precursor was made by further diluting titanium diisopropoxide bis(acetylacetonate) 75 wt% in 2-propanol with 2-propanol. The typical amounts were 1.5 ml of titanium diisopropoxide bis(acetylacetonate) 75 wt% per 6.5 ml 2-isopropanol. The precursor was deposited on the substrates by spraying 13 short cycles with 20 s between the cycles onto the substrates on a hotplate at 450 °C. After the final cycle the substrates were annealed for 45 min at the same temperature. The resulting thickness of the layer was 60 nm. The substrates were stored in sealed containers in darkness. Immediately before the PIM deposition, the substrates were treated with oxygen plasma (11 W) for 1 min.

The PIM layers were deposited by spin-coating inside the $N_2$ glove box. Before starting the spin-coating program (3000 rpm for 30 s, acceleration within 5 s) 40 µL of the precursor was pipetted onto the $TiO_2$ coated substrate. During the spin-coating, right before the point when the film starts to change color, 150 µL of 2-propanol was pipetted onto the rotating substrate. After spin-coating the substrates were moved to a 130 °C hotplate and annealed for 10 min.

A 20 mg $mL^{-1}$ poly(3-hexylthiophene-2,5-diyl) solution in chlorobenzene was used as the hole transport material. It was spin-coated dynamically, that is, at speed (2000 rpm for 30 s) onto the PIM films inside the $N_2$ glove box. The method was adapted from the literature.[70] The doping of the HTM was also attempted by following a method from literature[71] where the 20 mg $mL^{-1}$ P3HT solution was mixed in a 1:1 ratio with a 1 w% F4-TCNQ solution in chlorobenzene. The doped HTM solution was spin-coated with the same parameters as the non-doped HTM. Finally, the solar cell was completed by thermally evaporating a 100 nm thick gold contact under a $6 \times 10^{-6}$ mbar vacuum. Each substrate held 3 solar cells with an area of 20 $mm^2$ each.

*XRD*: High-resolution XRD patterns of the Sb-PIM thin film samples on glass substrates were collected using Cu $K_\alpha$ radiation with $\lambda = 1.5406$ Å on a Malvern Panalytical Empyrean Alpha 1 high-resolution X-Ray diffractometer (Malvern, UK). The crystal structures were drawn using the visualization system for the electronic and structural analysis (VESTA) program.[72]

*SEM*: The SEM images of the Sb-PIM films were recorded using a field emission scanning electron microscope Carl Zeiss Ultra 55 (operation was at 5 kV). EDS spectroscopy (Oxford Instruments X-MaxN 80 EDS) combined with (Zeiss UltraPlus FE-SEM) was employed to determine the elemental composition of the films.

*NMR Sample Preparation and Measurements*: To get enough of the required powders the NMR samples of CsMAFA-Sb were made by dropping 80 µL of the PIM precursor on a clean glass slide on a hotplate at 50 °C. After this the temperature of the hotplate was increased to 130 °C where the films were annealed for 15 min. The films were then scratched to a powder with the scalpel. The powders obtained were then weighed and redissolved in known amounts of deuterated DMSO.

The samples that contained neat powders and the mixtures of neat powders of the samples were made by weighing the powders in the ratio they would be in the CsMAFA-Sb precursor and dissolving them in known amounts of deuterated DMSO.

NMR spectra were measured on JEOL JNM-ECZ500R 500 MHz spectrometer (JEOL, Japan) equipped with the broadband Royal probe in DMSO-d6. The chemical shifts were referenced to the solvent residual signal. For quantitative measurements a known amount of diphenyl ether was added to a weighted sample, and the inter pulse delay was set to 1 min to allow for complete relaxation.

*XPS*: The XPS measurements were conducted in an ultrahigh vacuum (UHV) system. The perovskite films were prepared on fluorine


© 2022 The Authors. Advanced Energy Materials published by Wiley-VCH GmbH

16146840, 2023, 4, Downloaded from https://onlinelibrary.wiley.com/doi/10.1002/aenm.202203175 by University of Turku, Wiley Online Library on [03/02/2023]. See the Terms and Conditions (https://onlinelibrary.wiley.com/terms-and-conditions) on Wiley Online Library for rules of use; OA articles are governed by the applicable Creative Commons License

doped tin oxide (FTO) coated glass slides and let degas in a vacuum desiccator overnight before loading into the UHV system. XPS data were measured using non-monochromatized Al $K\alpha_{1,2}$ X-rays ($h\nu = 1486.6$ eV) generated by a twin anode X-ray source (8025 Twin anode X-ray source, V. G. Microtech) and a hemispherical electron spectrometer (CLAM4 MCD LNo5, V. G. Microtech). The chemical states of the elements were determined from the XPS spectra by least-squares fitting of asymmetric Gaussian–Lorentzian lineshapes after background subtraction. The analysis was made in CasaXPS software version 2.3.25PR1.0[73] using the Scofield photoionization cross sections as relative sensitivity factors.[74]

*UV–Vis, PL, and TRPL*: Absorption spectra of the Sb-PIM films were recorded using a dual-beam grating Shimadzu UV-1800 absorption spectrometer, Shimadzu Corporation, Kyoto, Japan. Steady-state PL spectra were recorded with a FLS1000 spectrofluorometer (Edinburgh Instruments, UK). The TRPL decays were measured using a time-correlated single photon counting (TCSPC) apparatus equipped with a Picoharp 300 controller and a PDL 800-B driver for excitation and a Hamamatsu R3809U-50 microchannel plate photomultiplier for detection in 90° configuration.

*Pump–Probe Measurements*: A Libra F laser system (Coherent Inc.) generated 800 nm light pulses at a repetition rate of 1 kHz, which was reduced to half by a chopper for the sample pumping. The pulse duration (time-resolution) was ≈100 fs, and the measurement system (ExciPro, CDP Inc.) consisted of a silicon CCD array for measurements in the visible wavelength range. The pump wavelength was adjusted by a Topas C optical parametric amplifier (Light Conversion Ltd.), and the white light continuum for the probe pulses was generated by a water-filled cuvette. In both reflectance and transmittance modes, the sample was tilted ≈8–10° to acquire the reflectance signal.

*J–V Measurements*: The *J–V* characteristics of the solar cells were recorded under the Sciencetech SS150-AAA solar simulator, set to 1-Sun (100 mW $cm^{-2}$) with a Newport KG5 filtered reference cell (91150-KG5 Reference Cell and Meter). The measurements were done with the Keithley 2450 source-monitor unit using a 4-wire setup in ambient conditions. The indoor *J–V* features were measured under the illumination from a Philips HUE WLED bulb (color-temperature was 4000 K). The WLED bulb was adjusted to an appropriate distance from the photovoltaic cell to achieve an illuminance of 1000 lux with the help of a PeakTech 5065 digital lux-meter. The corresponding power density of 0.46 mW $cm^{-2}$ was calculated using a combination of an optical spectrometer and an optical power measurement unit (Thorlabs S130VC).

*$V_{OC}$ Decay and Trap-Density Experiments*: For the $V_{OC}$ decay measurements, the photovoltaic devices were illuminated with the WLED (1000 lux) at open-circuit conditions. After the $V_{OC}$ reached a steady value, the illumination was turned off with a shutter, and the $V_{OC}$ decays were monitored using a potentiostat (Ivium Technologies B.V., Compact Stat). The trap density samples were made with the structure ITO|PEDOT:PSS|PIM|P3HT|$MoO_3$|Au. The PEDOT:PSS solution was made by diluting the PEDOT:PSS precursor with dimethylformamide in a 1:1 ratio. 150 µL of the solution was spin coated onto clean and etched 2 × 2 cm ITO substrates dynamically. The spin coating program was 3000 rpm for 40 s. The films were then annealed for 1 h at 150 °C. The Sb-PIM and P3HT layers were made as described above. An ≈6 nm thick $MoO_3$ and an 80 nm thick gold layer were subsequently thermally evaporated onto the substrates to complete the trap density samples. The samples were measured in darkness with the Keithley 2450 source-monitor unit using a 4-wire setup in ambient conditions.

*Computational Details*: On the crystal structures in Figure S16, Supporting Information, DFT[75] calculations with periodic boundary conditions (PBC) were performed employing the light-tier1 basis set of numerical atom-centered orbitals (NAO) for each atom,[76] as implemented in the Fritz Haber Institute ab initio molecular simulations (FHI-aims) code.[77] Within the Fritz Haber Institute ab initio molecular simulations (FHI-aims) framework, the electrons were described by the zero-order regular approximation (atomic ZORA). As self-consistency threshold for electron density convergence, a total energy criterion of $1 \times 10^{-6}$ eV was employed. The Perdew–Burke–Ernzerhof (PBE)[78] exchange correlation functional was employed for all geometry optimizations including the Tkatchenko–Scheffler (TS) correction[79,80] accounting for van der Waals dispersion forces . Our relaxed structures present maximum forces acting on each atom below 0.02 eV $Å^{-1}$. For the $Cs_3Sb_2I_9$, the Γ-centered (4 × 4 × 4) k-points sampling mesh had been used; these values ensure converged energies within 3 meV/f.u, while the (2 × 2 × 1) k-point scheme had been used for all the other structures. The mixed occupancy of Cs/MA/FA was simulated via the special quasi-random structure (SQS) approach as implemented in the Alloy Theoretic Automated Toolkit code.[81,82] The special quasi-random structure (SQS) is a state-of-the-art method to study solid solutions with two or more components and allowed our models to properly account for the configurational entropy by achieving a mixed occupancy.[83,84] Since the PBE functional usually underestimates the band energy gap, the HSE06 hybrid functional to calculate the projected density of states (pDOS) and the band energy structures on the PBE minimum-energy structures were employed.

## Supporting Information

Supporting Information is available from the Wiley Online Library or from the author.

## Acknowledgements

P.V. acknowledges the financial support of Jane and Aatos Erkko foundation within the SOL-TECH project and Academy of Finland (Decision No. 347772). M.L. thanks the Finnish Cultural Foundation (No. 00220107) for funding. This work is part of the Academy of Finland Flagship Programme, Photonics Research and Innovation (PREIN), Decision No. 320165. This work made use of Tampere Microscopy Center facilities at Tampere University. The authors thank Vipinraj Sugathan for the fruitful discussions.

## Conflict of Interest

The authors declare no conflict of interest.

## Data Availability Statement

The data that support the findings of this study are available from the corresponding author upon reasonable request.

## Keywords

2D-layered crystal structures, antimony, indoor photovoltaics, perovskite-inspired materials, triple-cation

Received: September 19, 2022
Revised: November 29, 2022
Published online: December 11, 2022

[1] B. Li, B. Hou, G. A. J. Amaratunga, *InfoMat* **2021**, *3*, 445.
[2] X. Hou, Y. Wang, H. K. H. Lee, R. Datt, N. Uslar Miano, D. Yan, M. Li, F. Zhu, B. Hou, W. C. Tsoi, Z. Li, *J. Mater. Chem. A* **2020**, *8*, 21503.
[3] I. Mathews, S. N. Kantareddy, T. Buonassisi, I. M. Peters, *Joule* **2019**, *3*, 1415.


© 2022 The Authors. Advanced Energy Materials published by Wiley-VCH GmbH

16146840, 2023, 4, Downloaded from https://onlinelibrary.wiley.com/doi/10.1002/aenm.202203175 by University of Turku, Wiley Online Library on [03/02/2023]. See the Terms and Conditions (https://onlinelibrary.wiley.com/terms-and-conditions) on Wiley Online Library for rules of use; OA articles are governed by the applicable Creative Commons License

[4] Y. Peng, T. N. Huq, J. Mei, L. Portilla, R. A. Jagt, L. G. Occhipinti, J. L. MacManus-Driscoll, R. L. Z. Hoye, V. Pecunia, *Adv. Energy Mater.* **2021**, *11*, 2002761.
[5] X. He, J. Chen, X. Ren, L. Zhang, Y. Liu, J. Feng, J. Fang, K. Zhao, S. Liu, *Adv. Mater.* **2021**, *33*, 2100770.
[6] E. L. Unger, L. Kegelmann, K. Suchan, D. Sörell, L. Korte, S. Albrecht, *J. Mater. Chem. A* **2017**, *5*, 11401.
[7] B. T. Muhammad, S. Kar, M. Stephen, W. L. Leong, *Mater. Today Energy* **2022**, *23*, 100907.
[8] J. Cao, F. Yan, *Energy Environ. Sci* **2021**, *14*, 1286.
[9] W. Ke, M. G. Kanatzidis, *Nat. Commun.* **2019**, *10*, 965.
[10] Z. Jin, Z. Zhang, J. Xiu, H. Song, T. Gatti, Z. He, *J. Mater. Chem. A* **2020**, *8*, 16166.
[11] K. Ruhle, M. Kasemann, *IEEE Photovoltaic Spec. Conf., 39th*, IEEE, Piscataway, NJ **2013**, pp. 2651.
[12] K. Yamada, H. Sera, S. Sawada, H. Tada, T. Okuda, H. Tanaka, *J. Solid State Chem.* **1997**, *134*, 319.
[13] B. Saparov, F. Hong, J. P. Sun, H. S. Duan, W. Meng, S. Cameron, I. G. Hill, Y. Yan, D. B. Mitzi, *Chem. Mater.* **2015**, *27*, 5622.
[14] J.-C. Hebig, I. Kuhn, J. Flohre, T. Kirchartz, *ACS Energy Lett.* **2016**, *1*, 309.
[15] F. Umar, J. Zhang, Z. Jin, I. Muhammad, X. Yang, H. Deng, K. Jahangeer, Q. Hu, H. Song, J. Tang, *Adv. Opt. Mater.* **2019**, *7*, 1801368.
[16] G. Li, J. Wu, J. Fang, X. Guo, L. Zhu, F. Liu, M. Zhang, Y. Li, *Chin. J. Chem.* **2020**, *38*, 697.
[17] C. Zuo, L. Ding, *Angew. Chem., Int. Ed.* **2017**, *56*, 6528.
[18] P. C. Harikesh, H. K. Mulmudi, B. Ghosh, T. W. Goh, Y. T. Teng, K. Thirumal, M. Lockrey, K. Weber, T. M. Koh, S. Li, *Chem. Mater.* **2016**, *28*, 7496.
[19] Y. Peng, F. Li, Y. Wang, Y. Li, R. L. Z. Hoye, L. Feng, K. Xia, V. Pecunia, *Appl. Mater. Today* **2020**, *19*, 100637.
[20] A. Hiltunen, N. Lamminen, H. Salonen, M. Liu, P. Vivo, *Sustainable Energy Fuels* **2022**, *6*, 217.
[21] Y. Yang, C. Liu, M. Cai, Y. Liao, Y. Ding, S. Ma, X. Liu, M. Guli, S. Dai, M. K. Nazeeruddin, *ACS Appl. Mater. Interfaces* **2020**, *12*, 17062.
[22] F. Jiang, D. Yang, Y. Jiang, T. Liu, X. Zhao, Y. Ming, B. Luo, F. Qin, J. Fan, H. Han, *J. Am. Chem. Soc.* **2018**, *140*, 1019.
[23] Y. K. Choi, J. H. Heo, K.-H. Hong, S. H. Im, *RSC Adv.* **2020**, *10*, 17724.
[24] N. Giesbrecht, A. Weis, T. Bein, *J. Phys. Energy* **2020**, *2*, 024007.
[25] F. Guo, S. Qiu, J. Hu, H. Wang, B. Cai, J. Li, X. Yuan, X. Liu, K. Forberich, C. J. Brabec, *Adv. Sci.* **2019**, *6*, 1901067.
[26] C. Pareja-Rivera, A. L. Solís-Cambero, M. Sánchez-Torres, E. Lima, D. Solis-Ibarra, *ACS Energy Lett.* **2018**, *3*, 2366.
[27] S. Cacovich, D. Messou, A. Bercegol, S. Béchu, A. Yaiche, H. Shafique, J. Rousset, P. Schulz, M. Bouttemy, L. Lombez, *ACS Appl. Mater. Interfaces* **2020**, *12*, 34784.
[28] K. X. Steirer, P. Schulz, G. Teeter, V. Stevanovic, M. Yang, K. Zhu, J. J. Berry, *ACS Energy Lett.* **2016**, *1*, 360.
[29] Y.-L. Liu, C.-L. Yang, M.-S. Wang, X.-G. Ma, Y.-G. Yi, *J. Mater. Sci.* **2019**, *54*, 4732.
[30] T. Geng, Z. Ma, Y. Chen, Y. Cao, P. Lv, N. Li, G. Xiao, *Nanoscale* **2020**, *12*, 1425.
[31] S. Berri, *Eur. Phys. J. B* **2020**, *93*, 191.
[32] J.-P. Correa-Baena, L. Nienhaus, R. C. Kurchin, S. S. Shin, S. Wieghold, N. T. Putri Hartono, M. Layurova, N. D. Klein, J. R. Poindexter, A. Polizzotti, *Chem. Mater.* **2018**, *30*, 3734.
[33] A. Koliogiorgos, S. Baskoutas, I. Galanakis, *Comput. Approaches Novel Condens. Matter Syst. [Proc. Gordon Godfrey Int. Workshop], 3rd* **2018**, *14*, 161.
[34] K. M. McCall, C. C. Stoumpos, S. S. Kostina, M. G. Kanatzidis, B. W. Wessels, *Chem. Mater.* **2017**, *29*, 4129.
[35] J. Mei, M. Liu, P. Vivo, V. Pecunia, *Adv. Funct. Mater.* **2021**, *31*, 2106295.
[36] J. Pal, S. Manna, A. Mondal, S. Das, K. V. Adarsh, A. Nag, *Angew. Chem., Int. Ed.* **2017**, *56*, 14187.
[37] B. Yang, K. Han, *J. Phys. Chem. Lett.* **2021**, *12*, 8256.
[38] M. Liu, S. Kasi Matta, H. Ali-Löytty, A. Matuhina, G. Krishnamurthy Grandhi, K. Lahtonen, S. P. Russo, P. Vivo, *Nano Lett.* **2021**, *22*, 311.
[39] Z. Yang, X. Wang, Y. Chen, Z. Zheng, Z. Chen, W. Xu, W. Liu, Y. M. Yang, J. Zhao, H. Zhu, *Nat. Commun.* **2019**, *10*, 4540.
[40] M. Liu, M. Endo, A. Shimazaki, A. Wakamiya, Y. Tachibana, *ACS Appl. Energy Mater.* **2018**, *1*, 3722.
[41] S. Makuta, M. Liu, M. Endo, H. Nishimura, A. Wakamiya, Y. Tachibana, *Chem. Commun.* **2016**, *52*, 673.
[42] B. Ghosh, B. Wu, X. Guo, P. C. Harikesh, R. A. John, T. Baikie, A. T. S. Wee, C. Guet, T. C. Sum, S. Mhaisalkar, *Adv. Energy Mater.* **2018**, *8*, 1802051.
[43] E. M. Hutter, M. C. Gélvez-Rueda, D. Bartesaghi, F. C. Grozema, T. J. Savenije, *ACS Omega* **2018**, *3*, 11655.
[44] H. C. Sansom, G. Longo, A. D. Wright, L. R. V. Buizza, S. Mahesh, B. Wenger, M. Zanella, M. Abdi-Jalebi, M. J. Pitcher, M. S. Dyer, *J. Am. Chem. Soc.* **2021**, *143*, 3983.
[45] V. Pecunia, Y. Yuan, J. Zhao, K. Xia, Y. Wang, S. Duhm, L. Portilla, F. Li, *Nano-Micro Lett.* **2020**, *12*, 27.
[46] K. J. Savill, A. M. Ulatowski, M. D. Farrar, M. B. Johnston, H. J. Snaith, L. M. Herz, *Adv. Funct. Mater.* **2020**, *30*, 2005594.
[47] M.-C. Wu, S.-H. Chan, M.-H. Jao, W.-F. Su, *Sol. Energy Mater. Sol. Cells* **2016**, *157*, 447.
[48] Y. Guo, J. Zhou, F. Zhao, Y. Wu, J. Tao, S. Zuo, J. Jiang, Z. Hu, J. Chu, *Nano Energy* **2021**, *88*, 106281.
[49] Q. An, F. Paulus, D. Becker-Koch, C. Cho, Q. Sun, A. Weu, S. Bitton, N. Tessler, Y. Vaynzof, *Matter* **2021**, *4*, 1683.
[50] J. Kim, J. H. Jang, E. Choi, S. J. Shin, J.-H. Kim, G. G. Jeon, M. Lee, J. Seidel, J. H. Kim, J. S. Yun, *Cell Rep.* **2020**, *1*, 100273.
[51] M. Saliba, L. Etgar, *ACS Energy Lett.* **2020**, *5*, 2886.
[52] Y. Zhang, M. Elawad, Z. Yu, X. Jiang, J. Lai, L. Sun, *RSC Adv.* **2016**, *6*, 108888.
[53] M. Liu, S. Dahlström, C. Ahläng, S. Wilken, A. Degterev, A. Matuhina, M. Hadadian, M. Markkanen, K. Aitola, A. Kamppinen, J. Deska, O. Mangs, M. Nyman, P. D. Lund, J.-H. Smått, R. Österbacka, P. Vivo, *J. Mater. Chem. A* **2022**, *10*, 11721.
[54] V. M. Le Corre, M. Stolterfoht, L. Perdigon Toro, M. Feuerstein, C. Wolff, L. Gil-Escrig, H. J. Bolink, D. Neher, L. J. A. Koster, *ACS Appl. Energy Mater.* **2019**, *2*, 6280.
[55] A. Singh, K. M. Boopathi, A. Mohapatra, Y. F. Chen, G. Li, C. W. Chu, *ACS Appl. Mater. Interfaces* **2018**, *10*, 2566.
[56] F. Bai, J. Zhang, A. Zeng, H. Zhao, K. Duan, H. Yu, K. Cheng, G. Chai, Y. Chen, J. Liang, *Joule* **2021**, *5*, 1231.
[57] G. K. Grandhi, S. Toikkonen, B. Al-Anesi, V. Pecunia, P. Vivo, *Sustainable Energy Fuels* **2023**, https://doi.org/10.1039/d2se00995a.
[58] G. K. Grandhi, B. Al-Anesi, H. Pasanen, H. Ali-Löytty, K. Lahtonen, S. Granroth, N. Christian, A. Matuhina, M. Liu, A. Berdin, V. Pecunia, P. Vivo, *Small* **2022**, *18*, 2203768.
[59] A. Zaban, M. Greenshtein, J. Bisquert, *ChemPhysChem* **2003**, *4*, 859.
[60] F. Di Giacomo, V. Zardetto, G. Lucarelli, L. Cinà, A. Di Carlo, M. Creatore, T. M. Brown, *Nano Energy* **2016**, *30*, 460.
[61] H. Yin, J. K. W. Ho, S. H. Cheung, R. J. Yan, K. L. Chiu, X. Hao, S. K. So, *J. Mater. Chem. A* **2018**, *6*, 8579.
[62] Y. Cui, Y. Wang, J. Bergqvist, H. Yao, Y. Xu, B. Gao, C. Yang, S. Zhang, O. Inganäs, F. Gao, *Nat. Energy* **2019**, *4*, 768.
[63] R. Steim, T. Ameri, P. Schilinsky, C. Waldauf, G. Dennler, M. Scharber, C. J. Brabec, *Sol. Energy Mater. Sol. Cells* **2011**, *95*, 3256.
[64] D. Glowienka, Y. Galagan, *Adv. Mater.* **2022**, *34*, 2105920.
[65] C. Teixeira, P. Spinelli, L. A. Castriotta, D. Müller, S. Öz, L. Andrade, A. Mendes, A. Di Carlo, U. Würfel, K. Wojciechowski, *Adv. Funct. Mater.* **2022**, 2206761.


© 2022 The Authors. Advanced Energy Materials published by Wiley-VCH GmbH

16146840, 2023, 4, Downloaded from https://onlinelibrary.wiley.com/doi/10.1002/aenm.202203175 by University of Turku, Wiley Online Library on [03/02/2023]. See the Terms and Conditions (https://onlinelibrary.wiley.com/terms-and-conditions) on Wiley Online Library for rules of use; OA articles are governed by the applicable Creative Commons License

[66] R. Cheng, C. Chung, H. Zhang, F. Liu, W. Wang, Z. Zhou, S. Wang, A. B. Djurišić, S. Feng, *Adv. Energy Mater.* **2019**, *9*, 1901980.
[67] X. Jiang, F. Wang, Q. Wei, H. Li, Y. Shang, W. Zhou, C. Wang, P. Cheng, Q. Chen, L. Chen, *Nat. Commun.* **2020**, *11*, 1245.
[68] H. Cheng, Y. Feng, Y. Fu, Y. Zheng, Y. Shao, Y. Bai, *J. Mater. Chem. C* **2022**, *10*, 13590.
[69] Q. Meng, Y. Chen, Y. Y. Xiao, J. Sun, X. Zhang, C. B. Han, H. Gao, Y. Zhang, H. Yan, *J. Mater. Sci.* **2021**, *32*, 12784.
[70] L. Yang, U. B. Cappel, E. L. Unger, M. Karlsson, K. M. Karlsson, E. Gabrielsson, L. Sun, G. Boschloo, A. Hagfeldt, E. M. J. Johansson, *Phys. Chem. Chem. Phys.* **2012**, *14*, 779.
[71] H.-C. V. Tran, W. Jiang, M. Lyu, H. Chae, *J. Phys. Chem. C* **2020**, *124*, 14099.
[72] K. Momma, F. Izumi, *J. Appl. Crystallogr.* **2011**, *44*, 1272.
[73] N. Fairley, V. Fernandez, M. Richard-Plouet, C. Guillot-Deudon, J. Walton, E. Smith, D. Flahaut, M. Greiner, M. Biesinger, S. Tougaard, *Appl. Surf. Sci. Adv.* **2021**, *5*, 100112.
[74] J. H. Scofield, *J. Electron Spectrosc. Relat. Phenom.* **1976**, *8*, 129.
[75] K. Burke, *J. Chem. Phys.* **2012**, *136*, 150901.
[76] V. Blum, R. Gehrke, F. Hanke, P. Havu, V. Havu, X. Ren, K. Reuter, M. Scheffler, *Comput. Phys. Commun.* **2009**, *180*, 2175.
[77] V. Havu, V. Blum, P. Havu, M. Scheffler, *J Comput Phys* **2009**, *228*, 8367.
[78] J. P. Perdew, K. Burke, M. Ernzerhof, *Phys. Rev. Lett.* **1996**, *77*, 3865.
[79] A. Tkatchenko, M. Scheffler, *Phys. Rev. Lett.* **2009**, *102*, 73005.
[80] A. Tkatchenko, R. A. DiStasio Jr, R. Car, M. Scheffler, *Phys. Rev. Lett.* **2012**, *108*, 236402.
[81] A. Van De Walle, M. Asta, G. Ceder, *Calphad* **2002**, *26*, 539.
[82] A. van de Walle, R. Sun, Q.-J. Hong, S. Kadkhodaei, *Calphad* **2017**, *58*, 70.
[83] A. Massaro, A. B. Munoz-Garcia, P. P. Prosini, C. Gerbaldi, M. Pavone, *ACS Energy Lett.* **2021**, *6*, 2470.
[84] A. Massaro, A. Langella, A. B. Muñoz-García, M. Pavone, *J. Am. Ceram. Soc.* **2022**, *106*, 109.


© 2022 The Authors. Advanced Energy Materials published by Wiley-VCH GmbH

16146840, 2023, 4, Downloaded from https://onlinelibrary.wiley.com/doi/10.1002/aenm.202203175 by University of Turku, Wiley Online Library on [03/02/2023]. See the Terms and Conditions (https://onlinelibrary.wiley.com/terms-and-conditions) on Wiley Online Library for rules of use; OA articles are governed by the applicable Creative Commons License